nature portfolio

https://doi.org/10.1038/s41567-021-01492-w

Supplementary information

Topological dissipation in a time-multiplexed photonic resonator network

In the format provided by the authors and unedited

Supplementary Information for "Topological Dissipation in a Time-Multiplexed Photonic Resonator Network"

Christian Leefmans[1,*], Avik Dutt[2,*], James Williams[3], Luqi Yuan[4], Midya Parto[3], Franco Nori[5,6], Shanhui Fan[2], Alireza Marandi[1,3,†]

[1]Department of Applied Physics, California Institute of Technology, Pasadena, CA 91125, USA.
[2]Department of Electrical Engineering, Stanford University, Stanford, CA 94305, USA.
[3]Department of Electrical Engineering, California Institute of Technology, Pasadena, CA 91125, USA.
[4]State Key Laboratory of Advanced Optical Communication Systems and Networks, School of Physics and Astronomy, Shanghai Jiao Tong University, Shanghai 200240, China.
[5]Theoretical Quantum Physics Laboratory, RIKEN, Wako-shi, Saitama 351-0198, Japan.
[6]Department of Physics, University of Michigan, Ann Arbor, Michigan 48109-1040, USA.

[*]These authors contributed equally
[†]marandi@caltech.edu

1 Detailed Explanation of the Experimental Procedure

In this section, we provide a detailed explanation of our experimental procedure. We first provide a high-level description of the network shown in Fig. 1. Then, to provide an exhaustive picture of how to construct and operate our experiment, we follow a pulses' trajectories through the network, discussing the effect of each element in Fig. 1 as we go along. After this, we briefly discuss the protocols used to calibrate the various modulators in the network, and, finally, we provide an in-depth discussion of our measurement procedures.

1.1 Overview of the Experimental Setup

Our basic network design consists of a long fiber loop, which we call the "main cavity." We divide the main cavity into time bins that are separated by the repetition rate of an input 1550 nm mode-locked laser. The repetition rate is 250 MHz, so that the pulse separation is T_R=4 ns. In

our experiment, we set the length of the main cavity so that it supports 64 time-multiplexed optical resonators.

To introduce topological behaviors into our network, we couple the pulses in the main cavity through four optical delay lines. The delay lines couple each pulse of the network to other pulses a fixed number of time bins away. To construct these delay lines, we insert a 1×8 splitter and a 1×8 combiner into the main cavity, and we construct additional paths between the splitter and the combiner that differ in delay by integer multiples of the pulse separation time relative to the section of the main cavity that lies between the splitter and the combiner. The delay lines shorter than the corresponding section of the main cavity (labeled with a "$-$" in Fig. 1) couple to "earlier" time bins, while the the delay lines longer than the corresponding section of the main cavity (labeled with a "$+$" in Fig. 1 couple to "later" time bins. For our experiments, we construct $\pm T_{\mathrm{R}}$ and $\pm 4T_{\mathrm{R}}$ delay lines.

The delay lines establish the lattice type and the coupling lengths present on the lattice, but to study topological tight-binding models we must also control the strength and phase of each coupling. Accordingly, we insert intensity modulators (IMs) and phase modulators (PMs) into the delay lines. These modulators set the intensities and phases of the network's couplings so that they correspond to the couplings of the topological model under study. For the models studied in this work, the Su-Schrieffer-Heeger (SSH) model and the Harper-Hofstadter (HH) model, it is only necessary to have either a phase modulator or an intensity modulator in each delay line. However, one could insert an IM and a PM into each delay line to enable greater control over the phase and intensity of each coupling.

1.2 Details of the Experimental Setup

Figure 1 details the optical, electronic, detection, and stabilization elements of our experiment. Many of these elements are interdependent, so, to explain Fig. 1, we will start from the 1550 nm mode-locked laser and follow each path to its terminus, discussing the components we encounter as we go.

The 1550 mode-locked laser produces a steady stream of pulses with a 250 MHz repetition rate. These pulses first encounter a 50:50 splitter, which divides each pulse evenly between two paths. Along the first of these paths, which is the leftmost path in Fig. 1, the pulses pass directly to a 1.2 GHz photodetector. We pass the output of this detector through a 300 MHz low pass filter, which isolates the 250 MHz component of the optical pulse train. We use this 250 MHz signal as a reference clock for the FPGA used to generate the experiment's modulator driving signals. Clocking the FPGA with a sinusoid derived directly from the optical signal reduces any drift between the FPGA's electronics and the optical pulses.

The full details of the FPGA's firmware are discussed elsewhere [1]. For the purposes of this discussion, all that matters is that we load modulator driving waveforms from a PC onto the various channels of the FPGA, and we use the computer to trigger each experiment. Upon a trigger event, the FPGA outputs the waveform stored on each output channel. This waveform passes through an amplification stage and is then transmitted to a certain modulator (see blue

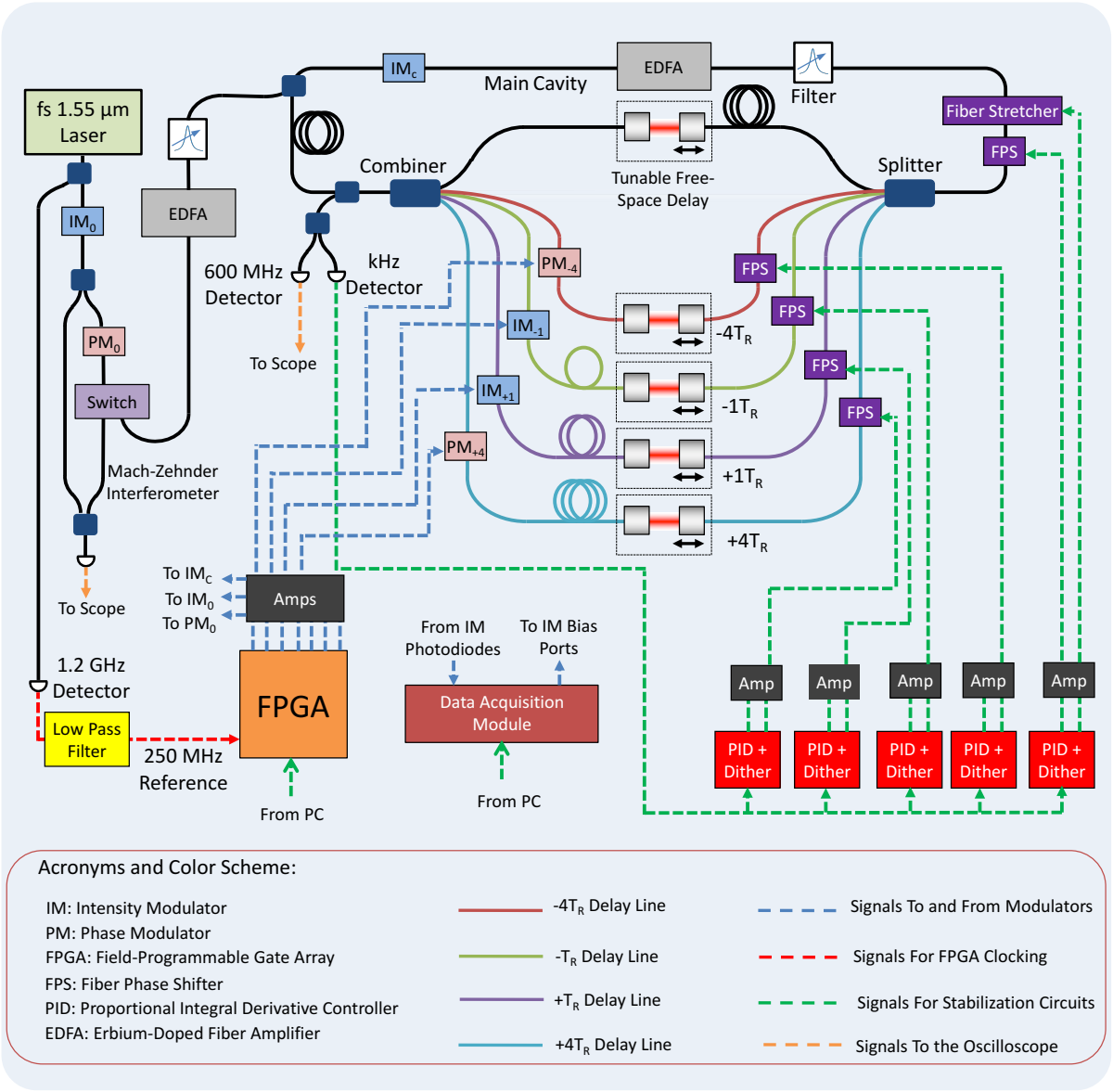

Figure 1: **Detailed schematic of the experimental setup.**

dashed arrows in Fig. 1), where it modulates the pulses either before or in the network. The amplitudes of the modulator driving waveforms are determined by a calibration procedure that will be discussed in Section 1.3.

Let us now return to the 1550 femtosecond laser in the top left corner of Fig. 1 and follow the path containing IM_0. Directly after this intensity modulator is a Mach-Zehnder interferometer (MZI) with PM_0 and a "switch" in one arm. This MZI is used to calibrate PM_0. In practice, we implement the switch manually unplugging the fiber pigtail of PM_0 from the input to the main cavity and connecting it to the MZI. This MZI is used to calibrate the phase vs. voltage response of PM_0.

Continuing along the input to the main cavity, we next encounter an EDFA. This EDFA, which sits before the main cavity increases the power in the main cavity without adding additional gain to the main cavity. Before adding this EDFA we found that the signal at the network's output was quite faint but that the network would go above threshold when we increased the gain with the intracavity EDFA. Adding the EDFA before the main cavity enabled us to increase our signal to noise ratio while remaining sufficiently below threshold. The filter directly after the EDFA removes amplified spontaneous emission (ASE) generated by the EDFA.

We now arrive at the input to the main cavity, located at the top of Fig. 1. Pulses enter the main cavity via a 90:10 splitter, which is configured so that 10% of the light from the laser is passed into the main cavity. After this 90:10 splitter, the pulses pass through the intracavity intensity modulator, IM_C, and the second EDFA, which compensates for losses in the main cavity and the delay lines. As with the first filter, the filter after the intracavity EDFA suppresses ASE noise. After the filter, the pulses pass through a fiber stretcher and a fiber phase shifter (FPS), which are used to stabilize the main cavity, before being split between the delay lines.

As mentioned above, the delay lines contain PMs or IMs that control the couplings between the pulses. The delay lines also contain FPSs for stabilization, and they, along with the section of the main cavity that lies between the splitter and the combiner, contain tunable free-space delays. These tunable delays and phase shifters provide coarse and fine control over the length of each optical path, respectively. This ensures that (1) that the main cavity is on resonance and that (2) the delay lines interfere with the pulses in the main cavity when they meet at the combiner. After the delay lines and the main cavity recombine, the pulses are passed to another 90:10 splitter, which passes 10% of the cavity power to the experiment's detectors. The remaining light returns to the first 90:10 splitter at the input, where 90% of the light recirculates through the main cavity.

At the output of the main cavity, we split our signal between two detectors using a 50:50 splitter. One detector is a "fast," DC-coupled, 600 MHz detector, which we use to measure the amplitudes of individual pulses. The second detector is a slow, kHz detector that is used to stabilize the various paths of the network. We note that the SSH edge state data in the main text was collected using an EDFA pre-amp and a DC-coupled 5 GHz biased detector in place of the 600 MHz detector.

To stabilize the main cavity and the four delay lines, we use a top-of-fringe dither locking scheme for each path [2]. The lock-in modules in Fig. 1, which are Red Pitaya STEMLabs, send

dither signals to the FPSs in each path. In order to minimize cross-talk between the locks, we choose the frequency of each dither signal so that no one signal is a harmonic of any other. The FPSs in each path dither the lengths of the paths at their respective dither frequencies, which slightly modulates the interferences within network. This modulation is picked up by the setup's slow detector, and the lock-in modules in Fig. 1 demodulate the detector signal to generate error signals that quantify each paths position relative to the constructive interference (top-of-fringe) condition. The error signals are then fed to the lock-in modules' built-in proportional-integral-derivative (PID) controllers, which produce feedback signals to stabilize their respective paths. In the case of the delay lines, we add the feedback signal to the dither signal, so that we dither the delay lines and perform feedback on the same FPSs. In the case of the main cavity, we dither an FPS (which permits a higher dithering frequency), but we apply the feedback signal to a fiber stretcher. The fiber stretcher has a greater range than the FPS and is more convenient for locking the main cavity, which is the longest path in the system.

The final element of Figure 1 is a National Instruments data acquisition tool (NI-DAQ), which sets the bias of the network's IMs. Using a custom graphical user interface (GUI), we can either manually set the bias voltage of each IM or automatically set its bias to enable maximum or minimum throughput. If we choose to allow maximum or minimum throughput, then the program monitors the output of IMs' built-in photodiodes and adjusts the bias accordingly. For the purposes of our experiments, we always bias $\mathrm{IM_C}$ and $\mathrm{IM_{\pm 1}}$ to maximize their throughput, and we bias $\mathrm{IM_0}$ to minimize its throughput. We picture the modulator driving signals as "opening" $\mathrm{IM_0}$ to let light into the cavity, while they selectively close the IMs in the network either partially or completely during the experiments.

1.3 Modulator Calibration

To observe meaningful results in our network, we must calibrate the responses of each modulator over a sufficient range of driving voltages. To mitigate the effects of long-term drifts in the setup's electronics, we perform our calibration procedure before each round of measurements.

To calibrate the IMs, we reconfigure the paths in Figure 1 so that, one-by-one, there is a direct path from the laser, through each IM, to the 600 MHz detector. Then, using $\mathrm{IM_0}$, we send 100 consecutive pulses through this path, while applying a 100 step voltage ramp to these 100 pulses. This ramp varies from some negative voltage value to its equal and opposite positive voltage value in equally spaced steps. We measure the amplitudes of these 100 pulses and apply a polynomial fit to generate an amplitude vs. voltage plot. For each IM, we use its amplitude versus voltage curve to select the proper driving voltages for a given experiment. Note that, to calibration $\mathrm{IM_0}$, we apply the same voltage ramp to $\mathrm{IM_0}$ and measure the resulting amplitude versus voltage plot.

To calibrate the phase modulators, we need a local oscillator to interfere each phase modulated pulse with. Furthermore, we must calibrate each phase modulator in-place to ensure that the timing information of the optical and electronic pulses is the same during the calibration as it is during the experiments. This is why we build the MZI around the input PM, $\mathrm{PM_0}$. For the

delay line modulators, we selectively block the free space portions of the delay lines to interfere either the $+4T_R$ delay line or the $-4T_R$ delay line with the main cavity. The main cavity therefore acts as reference path for these delay lines.

Once we have constructed an interferometer for each phase modulator, we calibrate it in much the same way that we calibrate the intensity modulators. We sweep the phase modulator driving voltage with the same 100 pulse sequence, and we use the measured amplitudes to generate an amplitude versus voltage curve. Then, using the maximum and minimum points of this curve as reference points, we convert the amplitude versus voltage curve into a phase versus voltage curve. We use this phase versus voltage curve to assign driving voltages to a given phase modulator in our experiments.

1.4 The Locking and Experiment Modes

To ensure that our optical network is stable during an experiment, we must run the dither locking scheme described in Section 1.2 prior to the experiment and then transition from this "locking mode" to an "experiment mode" to perform our experiment. We switch between these modes using the FPGA in Fig. 1, which outputs different modulator driving waveforms in the locking and experiment modes. In this section, we briefly detail the process of switching between the locking and experiment modes and discuss how the optical response of our network appears on our detector in the two modes. This section serves as a prelude to the next section, in which the optical response in the locking mode plays a key role in accepting or discarding experiment runs.

As briefly mentioned in Section 1.2, we bias IM_0 to minimize its throughput. This allows us to selectively open IM_0 to send pulses into the main cavity during the experiment mode. However, during the locking mode, we would like to steadily inject pulses into all of the network's paths so that we can generate usable error signals from the output of the slow detector. Therefore, in the locking mode, we program the FPGA to send a steady pulse train to IM_0 to allow all pulses to pass through the modulator. When the network is properly locked, we observe these pulses as a constant stream of roughly equal amplitude pulses on the fast detector and as a DC signal on the slow detector.

As we must change this input pulse pattern to run our experiments, we do not lock the paths of our network during the experiment mode. However, in practice this is not an issue, as the paths of our network drift on a millisecond timescale, while each experiment takes only a few microseconds. A greater concern is to ensure that residual pulses from the locking mode have completely dissipated before we inject pulses for an experiment. To avoid any overlap between the locking and experiment modes, the FPGA shuts off its output for a programmable period of time between exiting the locking mode and beginning the experiment mode. This closes IM_0 and gives the light in the network from the locking mode time to dissipate. The FPGA implements a similar delay after the experiment before it resumes the locking mode.

For a typical experiment run, we observe the tail end of the experiment mode on our fast detector, followed by our experiment mode. The tail end of the locking mode typically appears

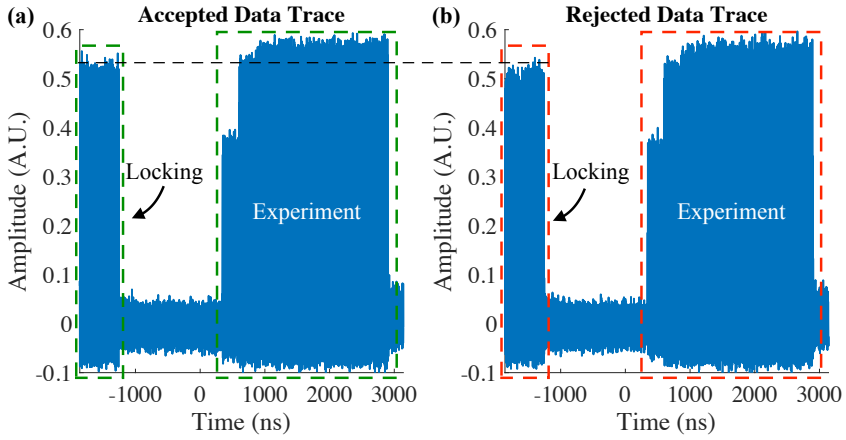

Figure 2: Example oscilloscope traces showing the locking and experiment modes and illustrating the measurement selection procedure. The amplitude during the locking cycle is slightly greater in (a) than in (b). The trace in (a) passes our measurement acceptance procedure, while the trace in (b) fails. Note that the individual pulses of the locking and experiment modes are not visible at the timescales in these plots.

as a constant stream of pulses that exponentially decays once the FPGA shuts off its input. The experiment cycle appears as an exponentially growing set of pulses that settle into a steady-state at some amplitude. Examples of such oscilloscope traces are shown in Fig. 2.

1.5 Setting a Threshold to Accept or Discard Band Structure Measurements

Our ability to record meaningful band structure data relies on our ability to determine when the optical network is stable. If any of the paths of the experiment "fall off lock" at the moment of our experiment, the relative phases of the pulses or the coupling phases of the delay lines will change and will introduce error into our measurement. To mitigate this error, we adopt a procedure to automatically cull data traces that fail to meet a certain "locking threshold," which we define as the metric by which we evaluate the stability of our experiment at any given time. In this section we introduce our locking threshold and discuss how we use it discriminate between "successful" and "unsuccessful" experiments.

In Section 1.4, we explained how the oscilloscope traces in Fig. 2 originated from the locking and experiment modes. Because all paths in the network are locked to constructive interference, the amplitudes of the pulses during the locking modes provide a sense of how stable the system is during the experiment mode. In particular, the fact that the amplitude of the pulses during the locking mode are lower in Fig. 2(b) than in Fig. 2(a) tells us that the system fell off lock before the experiment in Fig. 2(b). To efficiently collect data, we systematically reject data traces that exhibit "low" pulse amplitudes during the locking cycle.

To determine which traces should be discarded, we first establish a baseline amplitude for the pulses during the locking cycle. This is done by running an arbitrary experiment on the order of 50 times. For each experiment, we discard the data from the experiment mode and average the amplitudes of the pulses in the locking cycle. We take the maximum average pulse amplitude across these trials to be our baseline locking amplitude.

We next set a "threshold value" for discarding measurements. After collecting a data trace during an experiment, we only accept a data trace if the percent difference between the trace's average locking-mode amplitude and the baseline amplitude is less than the threshold value. For our SSH band structure measurements in the main text, we used a threshold of 2%. For our measurement in the topological phase, we achieved a measurement acceptance rate of 90%, while for our measurement at the phase transition point, we achieved a measurement acceptance rate of 86%.

For HH edge state measurements, we did not take advantage of this measurement selection scheme. However, given the high measurement acceptance rates of our band structure measurements, we do not believe the selection procedure would significantly change HH edge state results.

For the SSH phase transition and the SSH topological protection measurements, we used a threshold of 5%.

1.6 Experimental Procedure

We next discuss the procedures used to perform the band structure and edge state measurements. We will explain our measurement procedures in the contexts of the models studied in this paper, but the same procedures can be extended to other models that can be mapped to our network.

1.6.1 Band Structure Measurements

A diagram of our band structure measurement procedure is shown in Figure 3. The delay line couplings discussed above ensure that the eigenstates of our optical network are identical to those of the condensed matter tight-binding model under study. For reasons we shall explain in Section 3.1. We probe the eigenstates of the network by exciting them directly with the pulse stream input into the network.

We begin our band structure measurements by numerically calculating the Bloch wave eigenstates. We then generate the corresponding modulator driving signals to implement the desired couplings and to generate the Bloch wave eigenstates using the modulators at the input to the cavity. Because the SSH model with periodic boundary conditions (PBCs) exhibits discrete spatial translation symmetry, the amplitudes of the Bloch wave eigenstates are uniform, and we only need PM_0, the PM before the network, to produce each Bloch wave. Meanwhile, the two delay line IMs, $\mathrm{IM}_{\pm 1}$ implement the staggered couplings of the SSH model, while we disconnect the $\pm 4T_R$ delay lines to eliminate their couplings. Finally, we note that the intracavity IM, IM_C is unused for these band structure experiments. IM_C allows us to control the

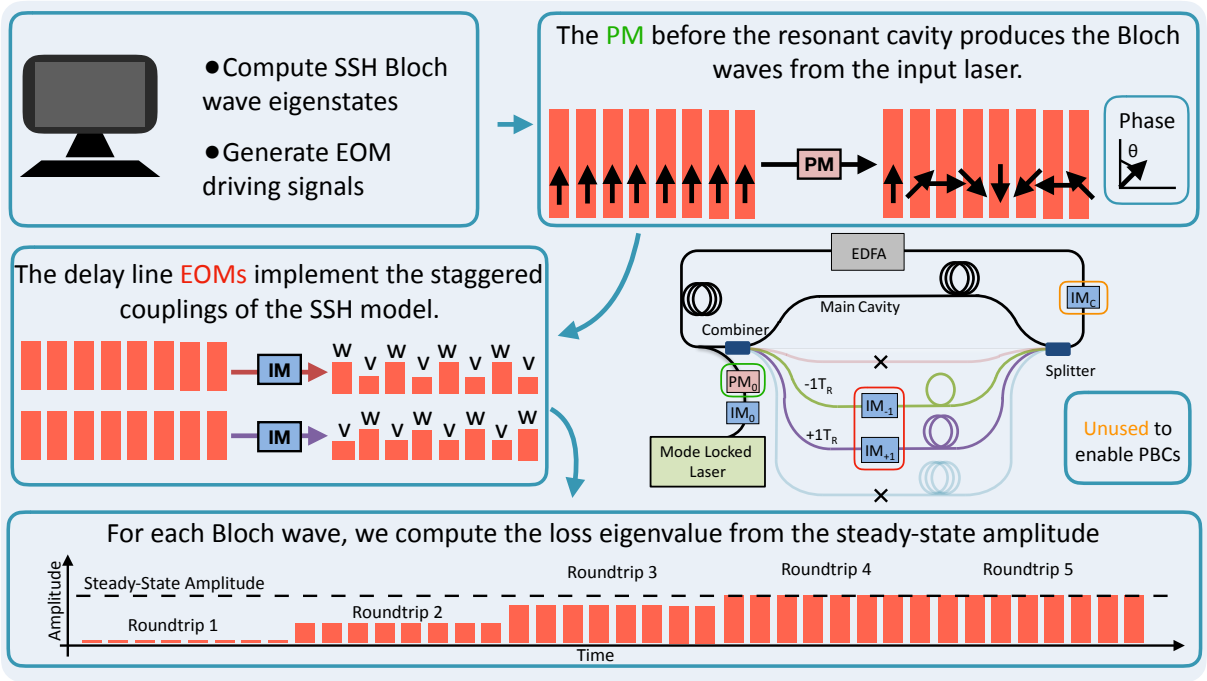

Figure 3: **Procedure used to measure the SSH band structure.**

boundary conditions or our synthetic lattice, and when it is unused, it enables PBCs in the network.

To execute the experiment, we excite a particular Bloch wave eigenstate of the network and record its steady-state amplitude. As we will discuss in Section 2, we can relate this steady-state amplitude to the photonic dissipation rate in the network. This dissipation rate maps directly to the energy of the SSH Hamiltonian.

We repeat this procedure for all 64 Bloch wave eigenstates of the system (there are 2 bands and 32 eigenstates per band). With the complete set of measured steady-state amplitudes, we generate a plot of steady-state amplitudes versus wavevector. Then, using the statistical procedure outlined in Section 2, we transform the measured amplitudes into the SSH band structure.

1.6.2 Edge State Measurements

Our edge state measurements follow a procedure similar to that of the band structure measurements, but there are a few differences. Here we will explain the edge state measurements in the context of the Harper-Hofstadter (HH) measurement. The SSH phase transition measurement discussed in the main text uses a nearly identical procedure, but the couplings are switched halfway through the experiment.

A diagram of the HH edge state measurement procedure is shown in Fig. 4. We begin this

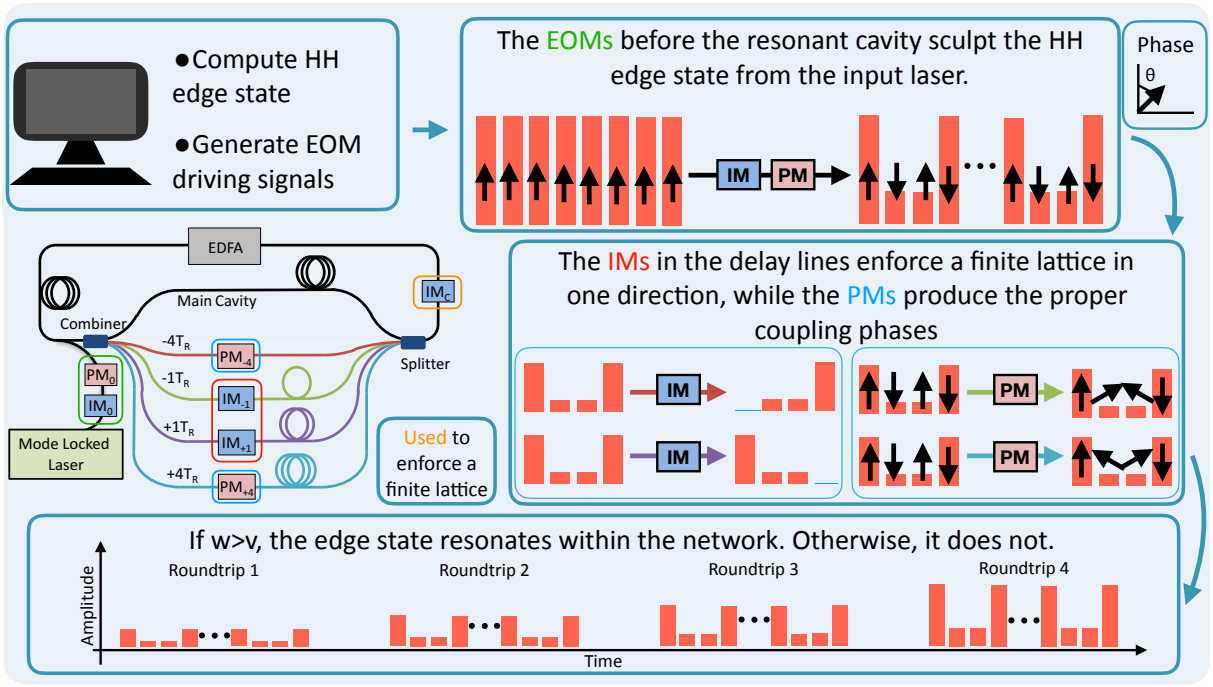

Figure 4: **Procedure used to measure the HH edge state.**

procedure by numerically calculating one of the HH edge states, and we generate the necessary modulator driving signals. The amplitudes of the edge state are not uniform, so we need to use both IM_0 and PM_0 to encode the HH edge state from the 1550 nm laser's output pulse stream.

When we work in the Landau gauge, we only need to apply hopping phases along one direction of our two-dimensional lattice to implement the HH model. We introduce these hopping phases with the PMs in the delay lines. Furthermore, as the hopping intensities are uniform in the HH model, we only need the delay line IMs to turn off certain couplings so that we can enforce finite boundary conditions along one direction of the synthetic lattice. While the delay line IMs implement finite boundary conditions along one direction, the intracavity IM, IM_C implements finite boundary conditions along the other by suppressing pulses in the main cavity. The effect of the IMs in the network is to ensure that we study a finite, 4×10 lattice in our experiments.

As with our band structure measurements, we excite the network directly with the HH edge states. When the delay line PMs are on and implement the correct phases, the edge state is an eigenstate of the system. Therefore, we expect the edge state to resonate within the network. However, when we turn off the delay line PMs, the edge state is no longer an eigenstate of the system, and the light should no longer remain localized in the edge state as it resonates within the network.

2 Band Structure Analysis

As described in Section 1.6.1, we measure the steady-state amplitudes of the optical network's Bloch wave eigenstates, and we fit the measured amplitude versus wavevector plot to transform the amplitudes into the SSH band structure. To extract a band structure from this type of measurement, we must consider the error associated with measuring the steady-state amplitudes of the individual eigenstates, the procedure used to fit the measured amplitudes, and the uncertainty bounds placed on our fit parameters. Each of these points present their own challenges, and we will address each of these challenges in turn.

2.1 A Single Amplitude Measurement

As we mentioned above, the Bloch wave eigenstates of the SSH model have uniform amplitudes because the 1D chain with PBCs exhibits discrete translation symmetry. Given this, we would expect that when we excite an eigenstate into the network, the resulting steady-state should also have a uniform amplitude. However, in our experiments we observe some deviation from this behavior for nonzero quasimomentum, k. In Fig. 5, we show two traces from the top band of our SSH band structure measurement at the phase transition point ($w = v$). Figs. 5(a) and (b) show the observed steady-state amplitudes of the SSH network at $k = 0$ and π respectively. While the steady-state amplitude is constant across the entire pulse train for $k = 0$, the steady-state amplitude of the Bloch wave at $k = \pi$ exhibits periodic oscillations. Note that the period of the oscillations are correlated with the phase rotation rate applied on PM_0, which indicates that the source of this discrepancy could be the phase errors on the input phase modulator PM_0. For example, the network response at $k = \pi$ exhibits oscillations with a period of approximately four pulses. This is the periodicity we would expect for a Bloch wave at $k = \pi$ on a two-site lattice like the SSH model.

To estimate the origin of this discrepancy, we simulate a simple 1D one-band model, $H_{1D} = J \sum_x a_{x+1}^\dagger a_x + \mathrm{H.C.}$ and look at the $k = \pi/4$ eigenstate excitation. In our experiment, a phase of $\phi = 0$ corresponds to PM_0 being almost completely off (in practice, what is considered $\phi = 0$ might be slightly shifted by the calibration). Therefore, we assume that the PM_0 implements $\phi = 0$ accurately but that it undershoots the remaining phases in the Bloch wave. For example, when $\phi > 0$, we imagine that the phase modulator actually implements $\phi - \alpha$, for some small $\alpha > 0$. With these phases, we simulate the measurement procedure described in Section 1.6.1. With $J = 0.1$, the intrinsic loss $\gamma = 0.4$, and $\alpha = \pi/10$, the resulting steady-state amplitude [Fig. 6] exhibits an oscillatory pattern similar to that observed in Fig. 5. These oscillations can be reduced by decreasing the coupling strength, J, or by reducing the phase undershoot. While the exact form of the phase error might be different, the qualitative agreement between Figs. 5 and 6 provides compelling evidence that the observed amplitude oscillations arise due to phase errors from PM_0.

To mitigate the effect of these pulse-to-pulse amplitude oscillations on the band structure measurements, we average over the pulse amplitudes of the steady-state network response. This

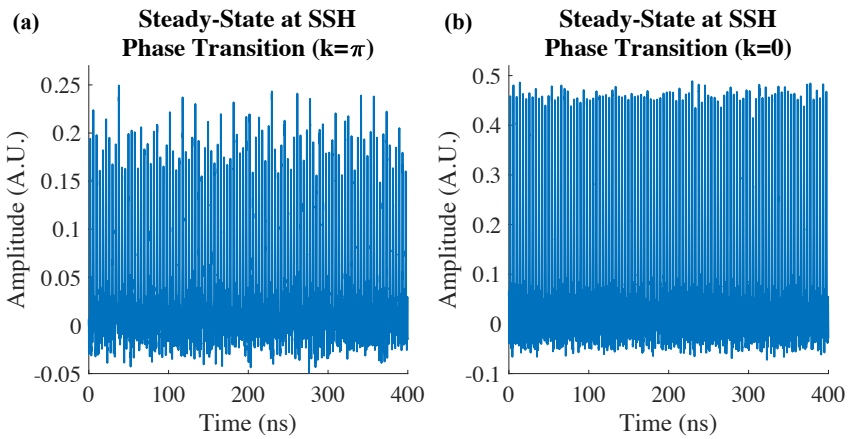

Figure 5: Observed traces showing the steady-state time traces of the network output in response to excitations with SSH Bloch wave eigenstates (a) at $k = \pi$ and (b) at $k = 0$.

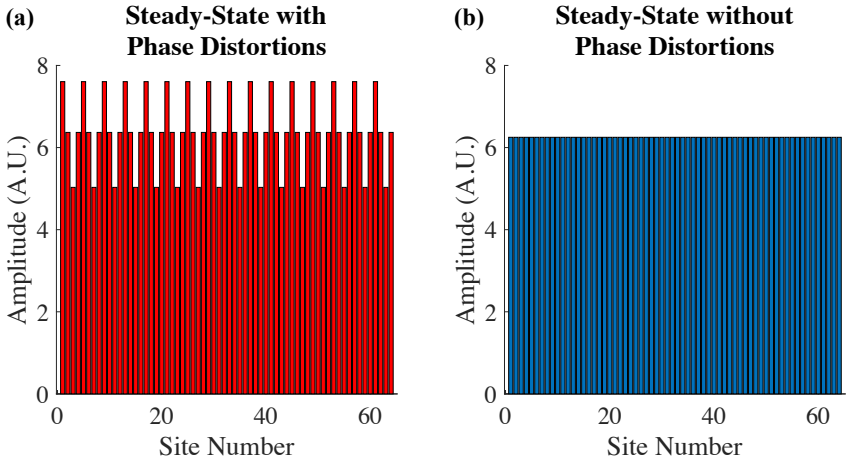

Figure 6: Simulated effect of input phase error on the network's steady-state response. This simulated conditions are discussed in the text.

procedure is justified by our simulations: despite the presence of amplitude oscillations, the average steady-state amplitude in Fig. 5(b) is only 1.5% from the expected steady-state amplitude. Our network reaches a steady-state after only 3 or 4 roundtrips, and a full experiment lasts 10 roundtrips. With this long of a steady-state, we select a large portion of these final 6 roundtrips to average over.

To generate more statistics for our band structure reconstructions, we acquire 5 data traces at each point on a band structure, using the procedure discussed in Section 1.5 to verify the stability of the network at measurement time. Using the same averaging window for each trace, we compute the averages of the pulse amplitudes and the standard errors of these averages. We use these averages and standard errors to reconstruct the band structure.

2.2 Reconstructing a Band Structure

Having devised a procedure to assign amplitudes to the measured steady states, we can now reconstruct the SSH band structure. To do this, we need a model to map the measured amplitudes to the eigenvalues of the SSH model, which correspond to the dissipation rates of the network's Bloch wave eigenstates. Recall that the dynamical equation of our network is

$$\frac{d\mathbf{a}}{dt} = (K - \gamma)\,\mathbf{a} + \mathbf{P}, \tag{1}$$

where the matrix K represents the couplings of the SSH model, γ represents the intrinsic optical losses, and $\mathbf{P}$ is a constant drive.

Note that if the dynamical matrix K is Hermitian, then it may also be thought of as an anti-Hermitian Hamiltonian. For example, if we temporarily neglect γ and $\mathbf{P}$, then we can rewrite Eq. 1 as $\partial_t \mathbf{a} = i(-iK)\mathbf{a}$. If K is Hermitian, then this equation is just the Schrödinger equation with the anti-Hermitian Hamiltonian $H = -iK$.

If the constant drive $\mathbf{P}$ is an eigenstate of the system, then we can diagonalize Eq. (1). As the network is initialized to zero amplitude, only one entry in the state vector is nonzero after diagonalization, and we can replace Eq. (1) by a single, scalar differential equation:

$$\frac{dc}{dt} = (\lambda - \gamma)\,c + \beta. \tag{2}$$

Here λ is the eigenvalue of K that corresponds to the eigenstate labeled by c. Solving for c, we find:

$$c = \frac{\beta}{\gamma - \lambda}\left(1 - e^{-(\lambda-\gamma)t}\right). \tag{3}$$

In our experiment, we measure $(|c|^2 + d)$ when $t \to \infty$, where d is the bias of our photodetector. Furthermore, to construct a fit model, we note that the β drive parameter can be absorbed into the denominator of Eq. (3). The resulting model is

$$|c|^2 = \frac{1}{(\Gamma - \Lambda)^2} + d. \tag{4}$$

For the SSH model, $\lambda = \pm\sqrt{w^2 + v^2 + 2wv\cos(k)}$, so we can express the specific model for our band structure measurements as

$$|c_\pm(k;\mathbf{x})|^2 = \frac{1}{\left(\Gamma \mp \sqrt{W^2 + V^2 + 2WV\cos(k)}\right)^2} + d, \tag{5}$$

where $W = w/\beta$ and $V = v/\beta$. In addition to being a function of k, we let $c_\pm$ be a function of the model parameters, $\mathbf{x} = (\Gamma, W, V, d)$. To reconstruct the SSH band structure, we use the Metropolis-Hastings algorithm to construct a posterior distribution for the fit parameters in Eq. (5). An advantage of using Markov chain Monte Carlo (MCMC) simulations to fit our data is that the simulations provide both estimates for the fit parameters and Bayesian confidence intervals for our estimates. Detailed descriptions of the Metropolis-Hastings sampler can be found elsewhere [3]; here we will simply summarize the steps used in our implementation of the algorithm.

We begin by defining a quantity called the acceptance ratio, A, defined as

$$A(\mathbf{x},\mathbf{y}) = \min\left(1,\ \frac{p(\mathbf{y})\mathcal{L}(\mathbf{d}|\mathbf{y})q(\mathbf{x},\mathbf{y})}{p(\mathbf{x})\mathcal{L}(\mathbf{d}|\mathbf{x})q(\mathbf{y},\mathbf{x})}\right). \tag{6}$$

Here $\mathbf{x}$ is a vector of the current model's parameters and $\mathbf{y}$ is a vector of a proposed model's parameters, $\mathcal{L}(\mathbf{d}|\mathbf{x})$ is the likelihood function for the data $\mathbf{d}$ given the model with parameters $\mathbf{x}$, and $p(\mathbf{x})$ is the prior distribution on the model parameters. The vector $\mathbf{y}$ is drawn from the proposal distribution, $q(\mathbf{x},\mathbf{y})$, which we take to be

$$q(\mathbf{x},\mathbf{y}) \propto \exp\left[-\frac{1}{2}\sum_i\left(\frac{|x_i - y_i|^2}{\eta_i^2}\right)\right] \tag{7}$$

for each fit parameter. The standard deviations, η_i, are parameters of the algorithm, and we shall return to these values momentarily. Because the proposal distribution, Eq. (7), is even with respect to $x_i - y_i$, the proposal distributions cancel in the numerator and denominator of Eq. (6).

To make use of the acceptance ratio in the Metropolis-Hastings algorithm, we must define the likelihood functions and the prior distribution. We assume that each measured amplitude is distributed according to a normal distribution to its sample mean, d_i and standard error, σ_i. Then the likelihood function can be written as

$$\mathcal{L}(\mathbf{d}|\mathbf{x}) \propto \exp\left[-\frac{1}{2}\sum_i\sum_{\alpha=\pm}\left(\frac{|d_i - c_\alpha(k_i;\mathbf{x})|^2}{\sigma_i^2}\right)\right] \tag{8}$$

where $c_\pm(k_i;\mathbf{x})$ is the fit model defined by Eq. (5) evaluated at the quasimomentum $k = k_i$ that corresponds to the measured amplitude, d_i.

There is considerably more latitude in our selection of the prior distribution. Given the best-fit values of the parameters and the physical restrictions on the possible parameter values (e.g.

the coupling parameters w and v should be positive), we selected the following prior distribution for the band structure measurement at the phase transition point:

$$p_{w=v}(\mathbf{x}) \propto \begin{cases} 0, & V < 0 \\ 0, & W < 0 \\ 0, & \Gamma \leq \sqrt{W^2 + V^2 + 2WV} \\ 1, & \text{Otherwise} \end{cases} \tag{9}$$

Note that we need not specify the constants of proportionality in Eq. (8) or Eq. (9). As with the proposal distribution, these constants will cancel in Eq. (6). For the band structure measurement in the topological phase, we add the additional constraint that $w > v$:

$$p_{w=v}(\mathbf{x}) \propto \begin{cases} 0, & V < 0 \\ 0, & W < 0 \\ 0, & W > V \\ 0, & \Gamma \leq \sqrt{W^2 + V^2 + 2WV} \\ 1, & \text{Otherwise} \end{cases} \tag{10}$$

This validity of this constraint is easily verified by measuring the coupling strengths of our network. Once again, we do not need to specify the constant of proportionality.

With the acceptance ratio and the distributions defined above, we run the Metropolis-Hastings algorithm, which consists of four basic steps:

1. Propose a set of model parameters, $\mathbf{y}$ from the proposal distribution $q(\mathbf{y}, \mathbf{x})$, where $\mathbf{x}$ is the set of current model parameters.

2. Compute $\log A(\mathbf{x}, \mathbf{y})$.

3. Generate a random variable, t from $\text{unif}\,(0, 1)$.

4. If $\log t \geq \log A\,(\mathbf{x}, \mathbf{y})$, the set $\mathbf{y}$ as the current model parameters. Otherwise, retain $\mathbf{x}$ as the current model parameters.

The "acceptance rate" (as opposed to the acceptance ratio) is defined as the rate at which we update the current model parameters in Step (4). This rate is set by the standard deviation of the proposal distribution in Eq. (7). We select $\eta_i = 0.0015$ for both band structure measurements to achieve an acceptance rate of 39.7% for the measurement in the topological phase and an acceptance rate of 31.3% for the measurement at the phase transition. Both acceptance rates lie within the recommended 20%-50% range [3].

To generate sufficient statistics to construct confidence intervals, we run the Metropolis-Hastings algorithm for 80,100,000 iterations. For each band structure measurement, we initialize the algorithm with the best fit model of our nonlinear regression algorithm and use a warm-up period of 100,000 iterations to ensure that our samples are independent of the initialization. After this warm-up period, we collect samples only every 40,000 iterations to decorrelate the

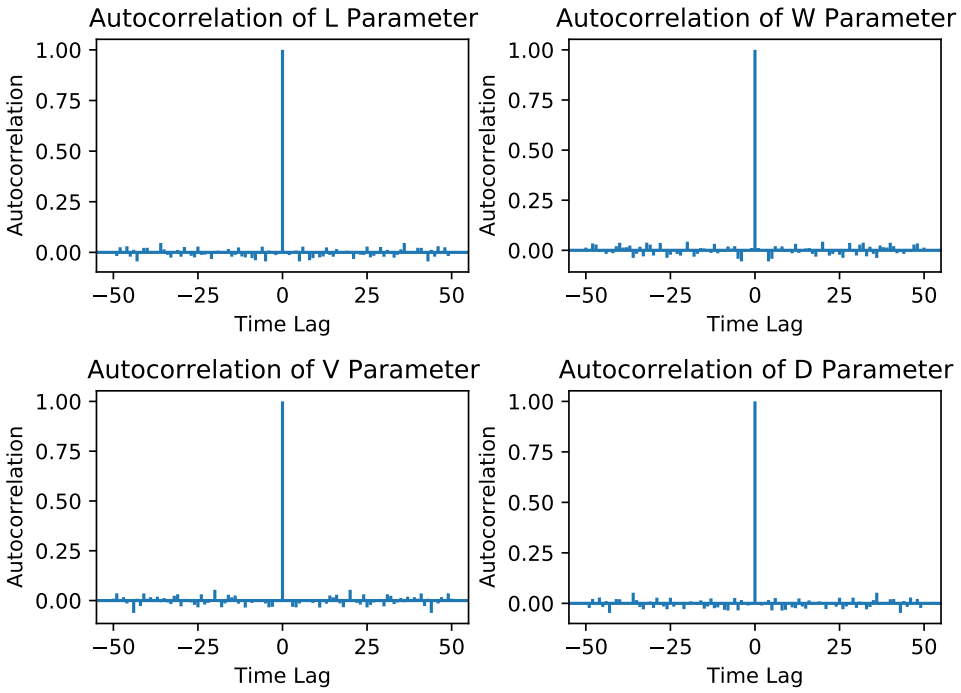

Figure 7: Autocorrelation plots for the Metropolis-Hastings algorithm run on the band measurement at the phase transition point.

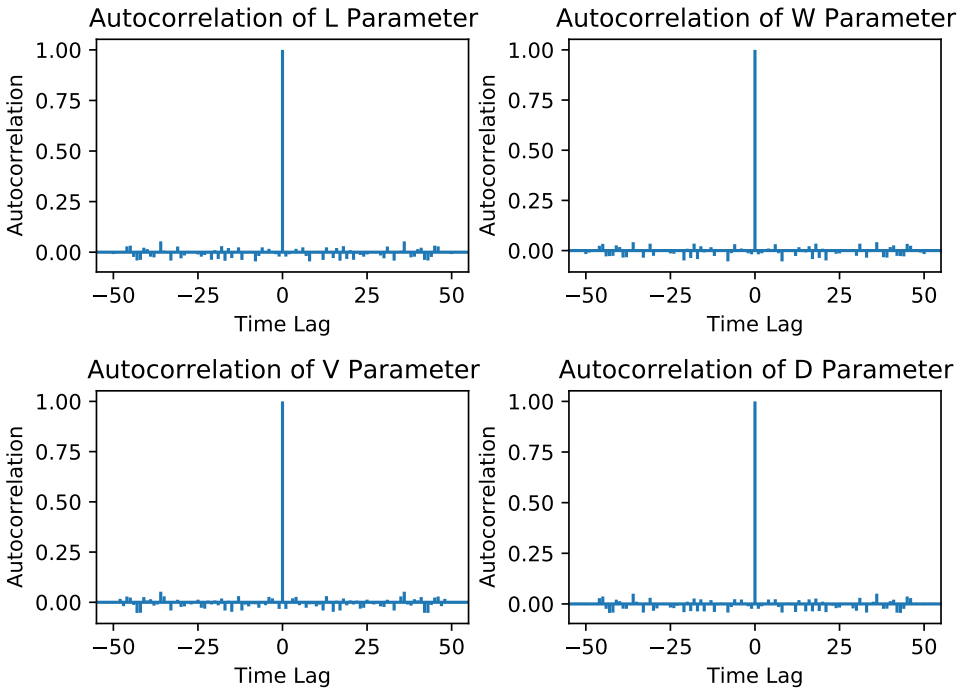

Figure 8: Autocorrelation plots for the Metropolis-Hastings algorithm run on the band measurement in the topological phase.

samples. The autocorrelation plots in Figs. 7 and 8 verify that the samples for each parameter are uncorrelated. With the chosen sampling rate, warm-up period, and total number of iterations, we collect a 2,000 samples, which we use to compute the means and 95% confidence intervals of the model parameters.

To quantitatively assess the quality of our band structure measurments, we are most interested in the ratio of the coupling parameters w and v, as this ratio indicates where our network lies relative to the topological phase transition. To estimate the mean coupling ratio $w/v = W/V$, we use the output of our MCMC simulations to construct a distribution for the ratio W/V. Then, we compute the mean and 95% confidence interval for this ratio. For the band structure measurement at the phase transition point, we find $W/V = 1.0\ (0.76, 1.25)$, and for the band structure measurement in the topological phase we find $W/V = 1.42\ (1.34, 1.49)$. The quantities in parentheses are the 95% confidence intervals for the extracted parameters. These numbers agree well with the expected values of 1.0 and $\sqrt{2} \approx 1.414$, which were the intended coupling ratios of the network during these measurements.

3 Conservatively and Dissipatively Coupled Resonator Arrays

In the main text, we analyzed our network with a Lindblad-like master equation. This approach illuminates connections between the dissipation engineering in our work and dissipation engineering in open quantum systems. Here we present a coupled mode theory of both conservatively and dissipatively coupled resonators to compare our dissipative time-multiplexed resonators with the conservatively coupled resonators previously studied in topological photonics. Afterwards, we discuss the possibility of using dissipative coupling to emulate conservative coupling within a certain bandwidth.

3.1 Coupled Amplitude Theory

Near resonance, systems of coupled resonators are well described by coupled-amplitude theory [4]. For a conservatively coupled resonator array, we can describe the dynamics within the coupled-amplitude approximation by,

$$\frac{d\mathbf{a}_c}{dt} = (iH - \gamma)\,\mathbf{a}_c + \mathbf{P}(t). \tag{11}$$

Here H is the coupling matrix, γ describes the optical losses of each resonator, and $\mathbf{P}(t)$ represents a time-varying drive. When $\gamma, \mathbf{P}(t) \to 0$, Equation (11) closely resembles the Schrödinger equation. In this limit, assuming that H is Hermitian, the solutions of Eq. (11) can be written as linear combinations of plane waves. On the other hand, for a dissipatively coupled resonator array, the dynamical equation within the coupled-amplitude approximation is

$$\frac{d\mathbf{a}_d}{dt} = (K - \gamma)\,\mathbf{a}_d + \mathbf{P}(t). \tag{12}$$

Equation (12)'s eigenfuctions are real exponentials when K is Hermitian. Here we explain how topological behaviors can arise in the dissipation of such a dissipatively coupled system.

For comparison, we first solve Eq. (11) to show that, by exciting a conservatively coupled system with a particular frequency ω, one predominantly excites eigenstates in the vicinity of that frequency ω. We transform Eq. (11) into a rotating frame by defining $\mathbf{a}_c = \tilde{\mathbf{a}}_c e^{i\omega t}$ and $\mathbf{P} = \tilde{\mathbf{P}} e^{i\omega t}$. We obtain

$$\frac{d\tilde{\mathbf{a}}_c}{dt} = \left[i(H-\omega) - \gamma\right] \tilde{\mathbf{a}}_c + \tilde{\mathbf{P}}(t). \tag{13}$$

Next, we diagonalize H by defining $H = S\Lambda S^{-1}$, with $\Lambda = \mathrm{diag}\{\dots, \lambda_i, \dots\}$. Defining $\mathbf{c} = S^{-1}\tilde{\mathbf{a}}_c$ and $\mathbf{P}_c(t) = S^{-1}\tilde{\mathbf{P}}(t)$, we find:

$$\frac{d\mathbf{c}}{dt} = \left[i(\Lambda-\omega) - \gamma\right] \mathbf{c} + \mathbf{P}_c(t). \tag{14}$$

Using the initial condition $c(t=0) = 0$, we solve Eq. 14 with an integrating factor and obtain

$$\mathbf{c}(t) = e^{[i(\Lambda-\omega)-\gamma]t} \int_0^t e^{-[i(\Lambda-\omega)-\gamma]t'} \mathbf{P}_c(t')\, dt'. \tag{15}$$

To evaluate the integral, we assume that $\mathbf{P}_c(t')$ varies on a slow time scale with respect to the loss rate γ. Then we can make the approximation $\mathbf{P}_c(t') = \mathbf{P}_c(0)$, and we can pull this term out of the integral. The remaining integral yields

$$\mathbf{c}(t) \approx \left(\frac{1 - e^{[i(\Lambda-\omega)-\gamma]}}{\gamma - i\left(\Lambda - \omega\right)}\right) \mathbf{P}_c(0). \tag{16}$$

Note that the prefactor multiplying $\mathbf{P}_c(0)$ is a diagonal matrix with entries

$$\frac{1 - e^{[i(\Lambda_{ii}-\omega)-\gamma]}}{\gamma - i\left(\Lambda_{ii} - \omega\right)} = \frac{1 - e^{[i(\lambda_i-\omega)-\gamma]}}{\gamma - i\left(\lambda_i - \omega\right)}, \tag{17}$$

where λ_i is the eigenvalue corresponding to the eigenstate, $c_i(t)$.

We are interested in squared projection of the system's state into one of the eigenstates, $c_i(t)$, which we can write as $|c_i(t)|^2$. At late times, this projection is given by

$$|c_i(t\to\infty)|^2 \approx \frac{1}{\left(\lambda_i - \omega\right)^2 + \gamma^2} |P_{ci}(0)|^2. \tag{18}$$

The frequency dependent factor is a Lorentzian of width 2γ. Therefore, in the conservatively coupled case, the projection $|c_i(t\to\infty)|^2$ depends on two things: the overlap of the drive, $\mathbf{P}_c$ with the ith eigenstate and the proximity of the driving frequency ω to the eigenvalue, λ_i. This calculation captures the essential content of conservatively coupled resonator arrays: Conservative coupling induces a frequency splitting in the eigenmodes of the system. When one drives the system at a certain frequency, one primarily excites the eigenstates within γ of the driving frequency.

For a dissipatively coupled system, we can solve Eq. (12) in a similar manner. We immediately diagonalize K by defining $K = S\Lambda S^{-1}$, $\mathbf{P}_d = S^{-1}\mathbf{P}(t)$ and $\mathbf{d} = S^{-1}\mathbf{a}_d$. With the initial condition $\mathbf{d}(t=0) = \mathbf{0}$, the solution reads,

$$\mathbf{d}(t) = e^{[\Lambda-\gamma]t} \int_0^t e^{-[\Lambda-\gamma]t'} \mathbf{P}_d(t')\, dt'. \tag{19}$$

We are interested in how we can excite a single eigenstate of the system, $d_i(t)$. When K corresponds to a topologically nontrivial Hamiltonian, this will tell us how to excite the edge state.

To bound the maximum "occupation" of a particular eigenstate, $d_i(t)$, given an arbitrary drive, $\mathbf{P}_d(t)$, we replace each element of $\mathbf{P}_d(t)$ by its maximum on the interval $[0, t]$. We can then perform the integral in Eq. (19) exactly to obtain the bound

$$|d_i(t)|^2 \leq \left(\frac{e^{[\lambda_i-\gamma]t} - 1}{\lambda_i - \gamma}\right)^2 \max\left\{|P_{di}(0 \leq t' \leq t)|^2\right\}. \tag{20}$$

In our experiments we use a constant drive, for which Equation (20) holds with equality. Furthermore, for Eq. (20) to hold in our experiments, our network must remain in the linear regime (i.e., below the lasing threshold), where $\lambda_l < \gamma,\ \forall\ \lambda_l$. We conclude that the projection $|d_l(t)|^2$ also depends on two things: the overlap of the drive $\mathbf{P}_d$ with the lth eigenstate and the eigenvalue, λ_l, which determines the loss rate of the lth eigenstate.

In the conservatively coupled case, the frequency of the drive, ω, "picked out" the eigenstates with eigenvalues near ω. However, in the dissipatively coupled case, the magnitude of $P_{dl}(t)$ (the projection of the driving term into the lth eigenstate) bounds the projection into $d_l(t)$. Now the influence of λ_l in Eq. (20) is to suppress the eigenstates with smaller eigenvalues, λ_l, more greatly than the eigenstates with larger λ_l. Let us now study the effect of this suppression, still limiting ourselves to the linear regime in which $\lambda_l < \gamma,\ \forall\ \lambda_l$. Assuming that the bound in Eq. (20) is tight, we can approximately express the ratio between the projections into the ith and jth eigenstates as $t \to \infty$ as

$$\left|\frac{d_i(t\to\infty)}{d_j(t\to\infty)}\right|^2 \approx \left(\frac{\lambda_j - \gamma}{\lambda_i - \gamma}\right)^2 \left(\frac{\max\left\{|P_{di}(0 < t' < t)|^2\right\}}{\max\left\{|P_{dj}(0 < t' < t)|^2\right\}}\right)^2. \tag{21}$$

If $|d_i(t\to\infty)|^2 = |d_{\text{top}}(t\to\infty)|^2$ corresponds to a topological edge state, then there exist states $|d_j(t\to\infty)|^2$ such that $\lambda_j > \lambda_i = \lambda_{\text{top}}$ because topological edge states occur in the gap between two bulk bands. Thus, to maximize the ratio $|d_{\text{top}}(t\to\infty)/d_j(t\to\infty)|^2$, we should minimize the second factor on the right-hand side of Eq. (21), that is, one must be careful not to excite other states with lower dissipation. Additionally, since the overall dissipation γ should be large enough to prevent the lowest-loss state from lasing (i.e., $\gamma \geq \max_j \lambda_j$), and the coupling constants J are inherently linked to the dissipation rates (see Section 5), it is not straightforward to achieve a large contrast $\left[(\lambda_{\text{top}} - \gamma)\,/\,(\lambda_j - \gamma)\right]^2$ for bulk states ($\lambda_j < \lambda_{\text{top}}$) below the band gap.

3.2 Emulating Conservative Coupling in Dissipatively Coupled Resonator Arrays

In this subsection, we analyze pairs of conservatively and dissipatively coupled resonators to show that, within a finite bandwidth, dissipative couplings can emulate the behaviors of conservative couplings. Our results suggest that, in future experiments, we might be able to study certain behaviors of conservatively coupled systems in our dissipatively coupled time-multiplexed resonator networks.

3.2.1 Coupled amplitude analysis

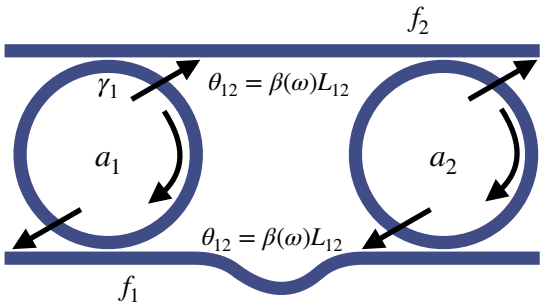

Figure 9: Two identical rings coupled by two connecting waveguides.

Consider the pair of identical ring resonators shown in Fig. 9, which are connected by two waveguide buses. The rings couple to the waveguides with a coupling strength γ_1, and the bus lengths, L_{12} and L_{21}, produce coupling phases $\theta_{12,21}(\omega) = \beta(\omega)L_{12,21}$ between the resonators. The equations for the mode fields inside the rings are,

$$\frac{\mathrm{d}}{\mathrm{d}t}a_1 = -2\gamma_1 a_1 + i\sqrt{2\gamma_1}\, f_1 \tag{22}$$

$$\frac{\mathrm{d}}{\mathrm{d}t}a_2 = -2\gamma_1 a_2 + i\sqrt{2\gamma_1}\, f_2, \tag{23}$$

where the two factors of γ_1 arise from the outcoupling of the resonators into the two buses, and the fields f_1 and f_2 describe the coupling between the resonators:

$$f_1 = i\sqrt{2\gamma_1}\, a_2 e^{i\theta_{21}}; \quad f_2 = i\sqrt{2\gamma_1}\, a_1 e^{i\theta_{12}}. \tag{24}$$

Note that we ignored the intrinsic losses of the waveguides in Eqs. (22)

Substituting the expressions for f_1 and f_2 in Eqs. (22), we obtain

$$\begin{pmatrix} \dot{a}_1 \\ \dot{a}_2 \end{pmatrix} = \begin{pmatrix} -2\gamma_1 & -2\gamma_1 e^{i\theta_{21}} \\ -2\gamma_1 e^{i\theta_{12}} & -2\gamma_1 \end{pmatrix} \begin{pmatrix} a_1 \\ a_2 \end{pmatrix}. \tag{25}$$

We can add gain g to each ring to partially compensate the diagonal loss terms. In this case the diagonal loss becomes $\gamma_0 = \gamma_1 - g$, and the coupling matrix takes the form,

$$\begin{pmatrix} -\gamma_0 & -2\gamma_1 \exp\left[i\theta_{21}\right] \\ -2\gamma_1 \exp\left[i\theta_{12}\right] & -\gamma_0 \end{pmatrix}. \tag{26}$$

Let us call the eigenvalues of this matrix $i\omega_{1,2}$, such that the system evolves with the time dependence $e^{i\omega_{1,2}t}$. We find,

$$\omega_{1,2} = -i\gamma_0 \pm i\sqrt{2\gamma_1}\, \exp\left[i(\theta_{12} + \theta_{21})/2\right]. \tag{27}$$

Note that the phases $\theta_{12,21}$ are themselves ω-dependent, so this equation must be solved in a self-consistent manner in the strong coupling regime. For $\theta_{12} + \theta_{21} = \pi$, the eigenvalues are real except for the overall loss $-i\gamma_0$. This corresponds to a split resonance, as would be expected for conservative coupling. Thus, when we set the locks such that the $+$ delay is constructive $\theta_{12} = 0$ and the $-$ delay is destructive $\theta_{21} = \pi$, we obtain conservative coupling. For $\theta_{12} + \theta_{21} = 0$, we get purely imaginary eigenvalues, as would be expected for dissipative coupling. This corresponds to setting the $+$ and $-$ delays both to constructive interference or both to destructive interference.

3.2.2 Scattering matrix method

In this section, we apply scattering matrices to systems of two identical, coupled resonators to illustrate how a dissipatively coupled system can emulate a conservatively coupled one. In general, we find that the frequency response of two dissipatively resonators can correspond exactly to that of two, lossy conservatively coupled resonators at a single frequency. Furthermore, within a certain bandwidth about this frequency, the frequency response of the dissipatively coupled resonators continues to closely resemble that of the conservatively coupled system, even though the correspondence is not exact. Specifically, we demonstrate that by properly engineering the coupling phases of the dissipatively coupled resonators, we can induce a frequency mode splitting analogous to the Autler-Townes effect in conservatively coupled resonators.

The layouts of two conservatively coupled resonators and two dissipatively coupled ring resonators are shown Fig. 10. The conservatively coupled resonators in Fig. 10(a) are evanescently coupled, while the dissipatively coupled resonators are coupled via a bus waveguide. While the coupling phase between the conservatively coupled resonators is fixed at $\pi/2$, it is possible to modify the coupling phases between the dissipatively coupled resonators by adjusting the lengths of the buses. We are interested in selecting these lengths so that the the frequency response of Fig. 10(b) emulates that of Fig. 10(a). For simplicity, here we consider the case in which the two buses have equal lengths.

We begin by analyzing the pair of identical, conservatively coupled resonators. To undertake this analysis, we label the field at different points in Fig. 10(a) by a_i, with $i = 0 \ldots 7$. Each label corresponds to the field either directly before or directly after the nearby coupling region. The power splitting ratio of the couplers are $T_1^2 : (1 - T_1^2)$ and $T_2^2 : (1 - T_2^2)$. We are interested

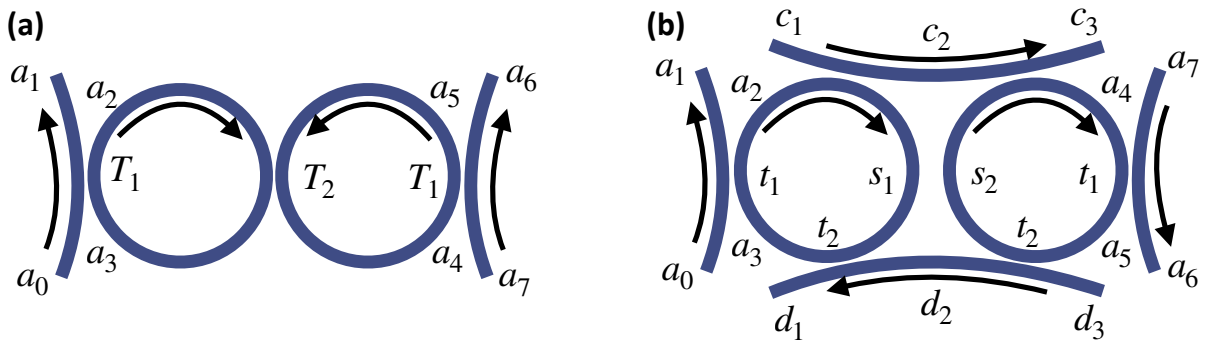

Figure 10: Rings coupled directly (conservative) vs. indirectly coupled via bus waveguides (dissipative).

in the frequency response of the field a_6 in response to an drive on the field a_0. By tracking the phases acquired through each section of the system, we find the following relation between the various fields of the system:

$$\begin{bmatrix} a_2 \\ a_3 \\ a_4 \\ a_5 \end{bmatrix} = \begin{bmatrix} 0 & \sqrt{1-T_1^2} & 0 & 0 \\ e^{i\theta_c}\sqrt{1-T_2^2} & 0 & 0 & iT_2e^{i\theta_c} \\ iT_2e^{i\theta_c} & 0 & 0 & e^{i\theta_c}\sqrt{1-T_2^2} \\ 0 & 0 & \sqrt{1-T_1^2} & 0 \end{bmatrix} \begin{bmatrix} a_2 \\ a_3 \\ a_4 \\ a_5 \end{bmatrix} + \begin{bmatrix} iT_1a_0 \\ 0 \\ 0 \\ 0 \end{bmatrix}. \tag{28}$$

Here $\theta_c = n\omega L/c - \gamma_c L$, where L is the length of the resonators, n is the index of refraction, ω is the optical frequency, and γ_c is the loss per unit length. The output field is given by $a_6 = iT_1a_4$.

To select the coupling phases for the dissipatively coupled system so that it emulates the conservatively coupled system, we perform a similar scattering matrix analysis for the resonators in Fig. 10(b). To maintain a consistent notation between the result of this analysis and the result of analyzing conservatively coupled system, we label the additional fields in Fig. 10(b) by q_i, r_i, and s_i. The transfer coefficients in Fig. 10(b) are t_1 and t_2. As in the conservatively coupled system, we can derive a relation between the fields of the system. We find

$$\begin{bmatrix} a_2 \\ a_3 \\ a_4 \\ a_5 \end{bmatrix} = \begin{bmatrix} 0 & \sqrt{1-t_1^2} & 0 & 0 \\ e^{i\theta_d}(1-t_2^2) & 0 & 0 & -t_2^2e^{i(\phi+\theta_d/2)} \\ -t_2^2e^{i(\phi+\theta_d/2)} & 0 & 0 & e^{i\theta_d}(1-t_2^2) \\ 0 & 0 & \sqrt{1-t_1^2} & 0 \end{bmatrix} \begin{bmatrix} a_2 \\ a_3 \\ a_4 \\ a_5 \end{bmatrix} + \begin{bmatrix} it_1a_0 \\ 0 \\ 0 \\ 0 \end{bmatrix}. \tag{29}$$

Here $\theta_d = n\omega L/c + i\gamma_d L$, where γ_d is the loss per unit length of the dissipatively coupled resonators. Note that we take the lengths of the conservatively and dissipatively coupled resonators to be equal, while we allow their intrinsic losses to differ. Furthermore, $\phi = n\omega\ell/c - \gamma_d\ell$, where

ℓ is the length of the buses. This equation shows that we can adjust the phase acquired through the buses by adjusting the lengths of the buses.

Armed with Eqs. (28) and (29), we want to solve for the parameters of the dissipatively coupled system that enable it to emulate the conservatively coupled system. To equate Eq. (28) and Eq. (29), there are three equations that we must satisfy:

$$\sqrt{1-T_1^2} = \sqrt{1-t_1^2} \tag{30a}$$

$$e^{i\theta_c}\sqrt{1-T_2^2} = e^{i\theta_d}\left(1-t_2^2\right) \tag{30b}$$

$$iT_2 e^{i\theta_c} = -t_2^2 e^{i(\phi+\theta_d/2)} \tag{30c}$$

From Eq. (30a) it is evident that $T_1 = t_1$. Meanwhile, the complex exponentials in of Eq. (30b) cancel because the lengths of the resonators are the same. The real exponentials of Eq. (30b) satisfy

$$\exp\left[-\gamma_c L\sqrt{1-T_2^2}\right] = \exp\left[-\gamma_d L\left(1-t_2^2\right)\right]. \tag{31}$$

To analyze Eq. (30c), we equate the magnitudes and phases separately. Equating the phases gives

$$e^{i\left(\frac{n\omega L}{2c}\right)} = e^{i\left(\frac{n\omega\ell}{c}+\frac{\pi}{2}\right)}, \tag{32}$$

which holds when

$$\begin{aligned}\ell &= L + \frac{2\pi c N}{n\omega} - \frac{\pi c}{2n\omega} \\ &= L + N\lambda/n - \lambda/4n,\end{aligned} \tag{33}$$

for $N \in \mathbb{Z}$. In the second line we have rewritten the condition on ℓ in terms of the wavelength. Written in terms of the wavelength, it is evident that the dissipatively coupled system only emulates the conservatively coupled system when the length of the bus exactly compensates for the additional $\pi/2$ phase accumulated when light couples into and out of the buses. Note that, in a more general analysis, in which we allow the lengths of the buses to be different, this condition becomes that the sum of the phases accumulated through the two buses must sum to π, which is exactly the result obtained with the coupled amplitude equations earlier.

Equation (33) tell us why we can only equate Eq. (28) and Eq. (29) at a single frequency: The lengths of the buses are fixed, so Eq. (33) only holds with equality at one frequency. However, for some bandwidth $\Delta\omega \ll \omega$, these equations will still hold approximately. Within this bandwidth, the dissipatively coupled system can emulate a conservatively coupled one.

Equating the magnitudes in Eq. (30c), we find that

$$T_2 e^{-\gamma_C(L/2)} = t_2^2 \exp\left[-\gamma_D\left(\ell + L\right)\right]. \tag{34}$$

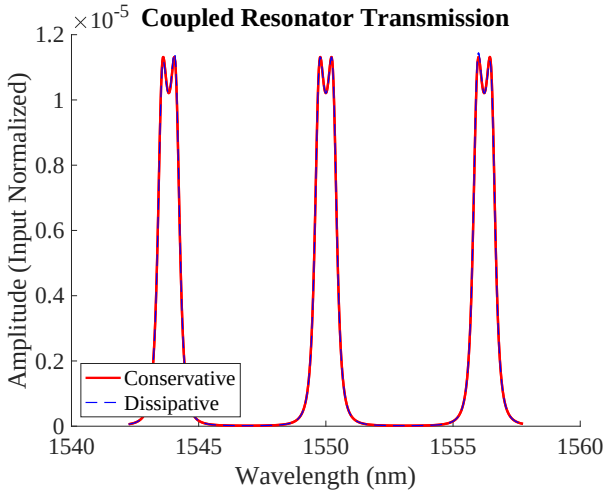

Figure 11: Emulating conservative coupling with dissipatively coupled resonators.

Using Eqs. (31), (33), and (34), we can solve for γ_d and t_2. We find

$$T_2 = \sqrt{\frac{x^2}{1+x^2}} \tag{35a}$$

$$\gamma_C = \gamma_D - \frac{1}{L}\ln\left(\frac{1-t_2^2}{\sqrt{1-T_2^2}}\right), \tag{35b}$$

where,

$$x = \frac{t_2^2}{1-t_2^2}\exp\left[-\gamma_D \ell\right]. \tag{36}$$

Equations. (35a) and (35b) can be inverted numerically to solve for t_2 and γ_D.

Eqs. (35a) and Eq. (36) provide an intuitive picture of how the conservatively coupled and dissipatively coupled systems are related. Using Eq. (35a) and Eq. (36) we can show that $(1-t_2^2)/\sqrt{1-T_2^2} < 1$ for $0 < t_2, T_2$. This allows us to conclude, from Eq. (35a), that $\gamma_c > \gamma_d$. In other words, the dissipatively coupled system always corresponds to a more lossy conservatively coupled system. This additional loss is to be expected, as the open ports in Fig. 10(b) behave like an additional source of loss in the dissipative system.

We have now shown in what sense a dissipatively coupled network can emulate a conservatively coupled one. By selecting the coupling phases of the dissipatively coupled network's bus waveguides properly, the frequency response of the dissipatively coupled system can approximate that of a conservatively coupled system over some bandwidth, with an exact correspondence holding at a particular frequency. As an example of this correspondence, we use the equations derived in this section to plot the frequency responses of a pair of dissipatively coupled resonators and the frequency responses of their conservatively coupled counterpart. These

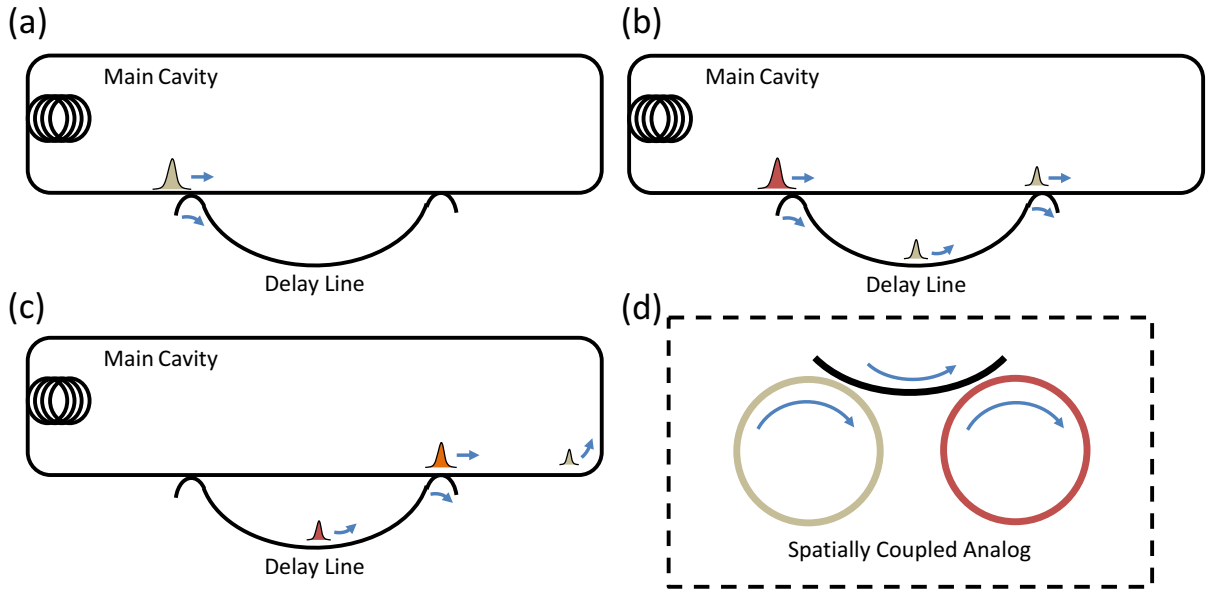

Figure 12: Illustration of a dissipative delay line coupling and its spatial analog in ring resonators.

plots are shown in Fig. 11. We see that the conservatively coupled and dissipatively coupled systems exhibit an Autler-Townes splitting. In addition, the responses of the dissipatively and conservatively coupled system are in excellent agreement overall several different resonances.

To end this section, we briefly contrast the conditions for the Autler-Townes splitting discussed above and those required to realize the optical analog of electromagnetically induced transparency (EIT) in pairs of dissipatively coupled resonators [5, 6, 7]. In the analysis above, we considered two identical resonators, and we induced a mode splitting by tuning the coupling phases between the resonators. In contrast, to achieve EIT-like behavior with two dissipatively coupled resonators, one must operate in a regime in which the coupling rate between the resonators is much larger than the detuning of the two resontors and in which the detuning of the two resonators is much larger than the intrinsic losses of the resonators [8]. This is very distant from the regime in which we performed the our analysis. Note that a separate set of conditions exist to realize EIT-like behavior with two conservatively coupled resonators [9].

3.3 Why Delay Lines Produce Dissipative Couplings

The dissipative nature of our delay line couplings in our photonic resonator network is essential to the experimental results presented in this work. Let us briefly discuss why these delay line couplings are dissipative.

As discussed above, two ring resonators coupled by bus waveguides are dissipatively cou-

pled, and the bus waveguides act as an intermediate reservoir that connects the two resonators. As illustrated in Fig. 12, the optical delay lines of a time-multiplexed network act analogously to bus waveguides for time-multiplexed resonators. Like all dissipative couplings, the delay line couplings of our network may be decomposed into two couplings: first a portion of one pulse is coupled into the modes of the optical delay line, and later a portion of this light is coupled back into another pulse in the network. In this way, the modes of the delay lines act as reservoirs that connect the pulses of our time-multiplexed system.

Figure 12 shows the correspondence between a delay line coupling between two photonic pulses and the bus waveguide coupling between two ring resonators. Figure 12(a-c) show the process by which the beige pulse couples to a later red pulse. In Fig. 12(a), the beige pulse is split between the delay line and the main cavity. The beige pulse continues along both paths, while in the meantime the red pulse reaches the splitter [Fig. 12(b)]. In Fig. 12(c), part of the beige pulse in the delay line couples to the red pulse in the main cavity, while the rest of the beige pulse in the delay line is lost through the open port. This coupling process is the time-multiplexed version of the coupled resonators shown in Fig. 12(d), in which the beige and red ring resonators are dissipatively coupled by a waveguide bus.

4 Robustness of the Dissipative Topological Edge State

In the main text we claim that our network exhibits "topological dissipation," by which we mean that topologically protected edge states occur in the band gap of the network's dissipation spectrum. These topological edge states are distinct from those that have been studied previously in topological photonics, which rely on optical analogs of the Schrödinger equation and which occur in the band gaps of a system's frequency spectrum. Given the novelty of the edge states studied in this paper, it is valid to wonder whether our topological edges states experience the same sort of topological protection. In this section, we show that the usual bulk-boundary correspondence applies to the dissipative topological models studied in this text.

We begin by reformulating the dynamical matrix that describes our dissipatively coupled system as an anti-Hermitian Hamiltonian. In particular, with no driving term and in the lossless limit, we can express the dynamics of our network as

$$\frac{d\mathbf{a}}{dt} = H\mathbf{a} \tag{37}$$

where H describes the coupling between sites. In practice, we choose H so that it corresponds to a Hermitian, tight-binding Hamiltonian.

We can rewrite Eq. (37) in analogy with the Schrödinger equation as follows:

$$i\frac{d\mathbf{a}}{dt} = A\mathbf{a}, \tag{38}$$

where $A = iH$ is a non-Hermitian Hamiltonian. We want to show that the spectra of A and H possess the same topological invariants.

Let us first consider the case in which H is the Hamiltonian of a static, noninteracting, 2D tight-binding model, so that the topology of H is described completely by the Chern number [4]. Recall that the Chern number of band i is given by

$$\mathcal{C}_i = \frac{1}{2\pi} \int_{BZ} d^2k \, \Omega_i \left(\mathbf{k} \right), \tag{39}$$

where $\Omega_i \left(\mathbf{k} \right)$ is the Berry curvature,

$$\Omega_i \left(\mathbf{k} \right) = i \nabla_{\mathbf{k}} \times \left\langle c_i \left(\mathbf{k} \right) \right| \nabla_{\mathbf{k}} \left| c_i \left(\mathbf{k} \right) \right\rangle . \tag{40}$$

Here $\left| c_i \left(\mathbf{k} \right) \right\rangle$ are the eigenstates of the reciprocal space representation of the Hamiltonian in the ith band. We will denote the reciprocal space representation of H as H_k. It follows that the reciprocal-space representation of A is $A_k = iH_k$.

Together, Eq. (39) and Eq. (40) tell us that the Chern numbers $\mathcal{C}_i$ depend only on the eigenvectors on H_k. Therefore, to evaluate the topological properties of our system, we should consider the eigenvalues and eigenvectors of A_k. From the relation $A_k = iH_k$ we immediately see that $\mathrm{spec} \left(A_k \right) = i \, \mathrm{spec} \left(H_k \right)$ and that the eigenvector of A_k corresponding to any eigenvalue $i\lambda_i \left(\mathbf{k} \right)$ is identical to the eigenvector of H_k corresponding to the eigenvalue $\lambda_i \left(\mathbf{k} \right)$. This property enables us to conclude that, if H_k has N bands, then A_k has N bands that are identical up to a factor of i. Furthermore, because H_k and A_k have the same eigenvectors, it is evident that the bands of H_k have the same Chern numbers as A_k. Therefore, we conclude that the edge states of A_k are guaranteed by the same bulk-boundary correspondence that guarantees the edge states of H_k. In other words, our dissipative network also exhibits topologically protected edge states.

We can make a similar argument regarding the SSH model. In particular, the topological invariant of the SSH model is the winding number [10], which can be calculated as:

$$\mathcal{W} = \frac{1}{2\pi} \int \left(\frac{\mathbf{h}(k)}{|\mathbf{h}(k)|} \times \frac{d}{dk} \frac{\mathbf{h}(k)}{|\mathbf{h}(k)|} \right) \cdot \hat{\mathbf{z}} \, dk, \tag{41}$$

where $\mathbf{h}(k)$ is defined in terms of the SSH Hamiltonian as $H_{\mathrm{SSH}} = \mathbf{h}(k) \cdot \sigma$. Once again, this topological invariant depends only on the eigenstates of the Hamiltonian. Similar arguments to those used above establish the validity of the bulk-boundary correspondence in this instance.

The arguments above frame the bulk-boundary correspondence in terms of a Schrödinger-like equation to draw a connection with the more common, Hamiltonian manifestations of topological photonics, but this procedure is contrived. The topological properties of the linear, time-independent system considered here are defined entirely by the time-independent eigenstates of that system. As long as these eigenstates are the eigenstates of a topologically nontrivial Hamiltonian, one can define a topological invariant with Eq. (39) or Eq. (41). The details of the time-evolution determine how the states of a system evolve, but they leave the topology intact.

To further elucidate the notion of dissipative topological protection, we examine the fluctuations in the optical power stored in the topological edge state $|\psi_0\rangle$ arising in the SSH lattice

implemented in our arrangement in the presence of random coupling disorders. In this scenario, one can write

$$\frac{d}{dt}\left|\psi_0\right\rangle = H_{SSH}\left|\psi_0\right\rangle + \Delta H\left|\psi_0\right\rangle = -\lambda_0\left|\psi_0\right\rangle + \Delta H\left|\psi_0\right\rangle, \tag{42}$$

where H_{SSH} is the unperturbed SSH Hamiltonian while $|\psi_0\rangle$ represents the edge-state wavefunction with its corresponding eigenvalue $-\lambda_0$. In addition, ΔH signifies a random coupling perturbation given by the matrix representation (here without loss of generality we consider a half-infinite left-edge eigenstate)

$$\Delta H = \begin{bmatrix} 0 & \delta\kappa_1 & 0 & 0 & ... \\ \delta\kappa_1 & 0 & \delta\kappa_2 & 0 & ... \\ 0 & \delta\kappa_2 & 0 & \delta\kappa_3 & ... \\ 0 & 0 & \delta\kappa_3 & 0 & ... \\ ... & ... & ... & ... & ... \end{bmatrix}. \tag{43}$$

Under such conditions, the time evolution of the edge-mode optical power stored within the cavity is given by

$$\frac{d}{dt}\left\langle\psi_0|\psi_0\right\rangle = -2\lambda_0\left\langle\psi_0|\psi_0\right\rangle + \left\langle\psi_0|\Delta H|\psi_0\right\rangle + \left\langle\psi_0|\Delta H^\dagger|\psi_0\right\rangle. \tag{44}$$

We now claim that for any off-diagonal matrix ΔH (corresponding to perturbations in the coupling coefficients of the 1D lattice) $\langle\psi_0|\Delta H|\psi_0\rangle = 0$. This can be shown by expanding ΔH in terms of its columns $\Delta H = \begin{bmatrix}\mathbf{C_1} & \mathbf{C_2} & ... & \mathbf{C_n} & ...\end{bmatrix}$ and by making the observation that $\langle\psi_0|\mathbf{C_n}\rangle = (-1)^{(n/2-1)}e^{-(n/2-1)p} \times \delta\kappa_{n-1} + (-1)^{(n/2)}e^{-(n/2)p} \times \delta\kappa_n$, when n is even while it vanishes for the odd values of n. This observation is based on the alternate site occupation of the topological edge state in the SSH model, i.e. the amplitude identically vanishes in sublattice B (odd sites) if the edge state starts on sublattice A (even sites). Here, p is the extinction ratio associated with the exponentially decaying edge state. Subsequently,

$$\left\langle\psi_0|\Delta H|\psi_0\right\rangle = \begin{bmatrix}0 & \delta\kappa_1 - e^{-p}\times\delta\kappa_2 & 0 & -e^{-p}\times\delta\kappa_3 + e^{-2p}\times\delta\kappa_4 & 0 & ...\end{bmatrix} \times \begin{bmatrix} 1 \\ 0 \\ -e^{-p} \\ 0 \\ e^{-2p} \\ ... \end{bmatrix} = 0. \tag{45}$$

Similarly, one can show that $\left\langle\psi_0|\Delta H^\dagger|\psi_0\right\rangle = 0$. Hence,

$$\frac{d}{dt}\left\langle\psi_0|\psi_0\right\rangle = -2\lambda_0\left\langle\psi_0|\psi_0\right\rangle. \tag{46}$$

This clearly indicates that the optical power associated with the topological edge state of the SSH lattice is robust against any coupling disorders.

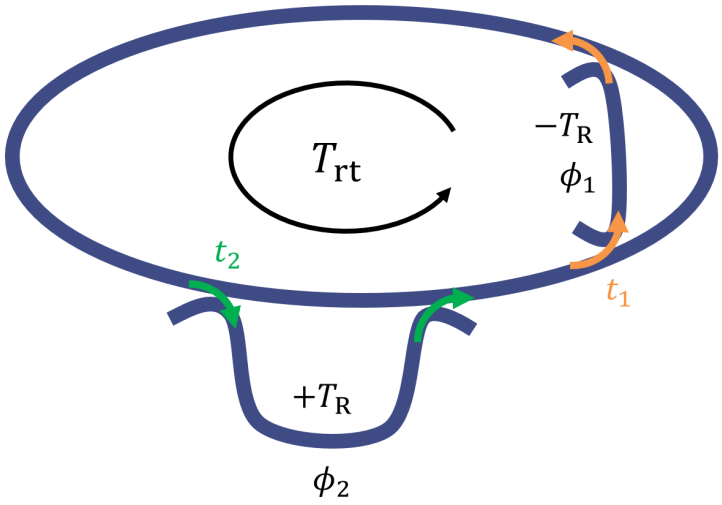

Figure 13: Schematic of $\pm T_{\mathrm{R}}$ delay lines for creating a 1D tight-binding lattice with nearest neighbor coupling in the time-multiplexed resonator. T_{rt} is the roundtrip time. t_1 and t_2 are the amplitude splitting ratios of the delay line couplers, which accumulate phases of ϕ_1 and ϕ_2 respectively.

5 Formalism of time-multiplexed dissipatively coupled networks of resonators

In this section, we establish a Lindblad-like master equation for the dynamics of time-bin modes in our resonator with optical delay line couplings. For simplicity, we will describe explicitly the case of two $\pm T_R$ delay lines, which represent a model with nearest-neighbor coupling in 1D [Fig. 13].

The finite difference equations for the j-th time-bin mode a_j, after one roundtrip T_{rt} through the main ring, can be written as,

$$a_j(t+T_{\mathrm{rt}}) = (1-t_1^2)\,(1-t_2^2)\,a_j(t) + (it_1)^2 e^{i\phi_1}\,a_{j+1}(t) + (it_2)^2 e^{i\phi_2}\,a_{j-1}(t) \tag{47}$$

Assuming the change in the field in each roundtrip is small, which is the case when the splitting ratios of the delay line couplers $t_1^2, t_2^2 \ll 1$, we obtain,

$$T_{\mathrm{rt}}\,\dot{a}_j = (-t_1^2 - t_2^2)\,a_j(t) - t_1^2 e^{i\phi_1} a_{j+1}(t) - t_2^2 e^{i\phi_2} a_{j-1}(t) + \mathcal{O}(t_1^2 t_2^2) \tag{48}$$

From this equation, we can read off the effective inter-site coupling terms $K_{j,j+1} = -it_1^2 e^{i\phi_1}/T_{rt}$, $K_{j+1,j} = -it_2^2 e^{i\phi_2}/T_{rt}$. Following the treatment of Ref. [11], we can write the (Hermitian/conservative) Hamiltonian coupling as $\mathcal{H} = \sum_j (J a_j^\dagger a_{j+1} + J^* a_j a_{j+1}^\dagger)$, with

$$J = (K_{j,j+1} + K_{j+1,j}^*)/2 \tag{49}$$

Note that here J is in general complex, since we have not made any assumptions about $t_1, t_2, \phi_1,$ and ϕ_2.

The anti-Hermitian part or the dissipative coupling can be written as,

$$\Gamma e^{-i\theta} = (K_{j,j+1} - K^*_{j+1,j}) \tag{50}$$

The Lindblad-like master equation for the system density matrix in the Schödinger picture for such a time-multiplexed resonator network is then

$$d\rho/dt = -i[\mathcal{H}, \rho] + \sum_j \mathcal{D}[L_j]\rho \tag{51}$$

where the dissipator, $\mathcal{D}[L_j]\rho = L_j \rho L_j^\dagger - \{L_j^\dagger L_j, \rho\}/2$, and the nonlocal jump operator, $L_j = \sqrt{\Gamma}\,(a_j + e^{-i\theta} a_{j+1})$, has a dissipative coupling rate Γ between neighboring sites.

To gain more insight about the role of t_1 and t_2 and the phases ϕ_1 and ϕ_2, let us assume that $t_1^2/T_{\rm rt} = t_2^2/T_{\rm rt} = \Gamma_0$. Then,

$$J = \Gamma_0\, e^{i(\phi_1+\phi_2)/2} \sin\left(\frac{\phi_1 - \phi_2}{2}\right) \tag{52}$$

$$\Gamma e^{-i\theta} = -i2\Gamma_0\, e^{i(\phi_1+\phi_2)/2} \cos\left(\frac{\phi_1 - \phi_2}{2}\right). \tag{53}$$

Thus, $\Gamma = 2\Gamma_0 \cos((\phi_1 - \phi_2)/2)$, $\theta = (\pi - \phi_1 - \phi_2)/2$ and $J = |J| \exp(i(\pi/2 - \theta))$ with $|J| = \Gamma_0 \sin((\phi_1 - \phi_2)/2)$. Let us look at a few special cases:

1. $\phi_1 = 0, \phi_2 = \pi$:
   $\Rightarrow |J| = \Gamma_0,\ \Gamma = 0$. *Purely Hermitian Hamiltonian* dynamics.

2. $\phi_1 = 0, \phi_2 = 0$:
   $\Rightarrow |J| = 0,\ \Gamma = 2\Gamma_0, \theta = \pi/2$. *Purely dissipative Lindbladian* dynamics.

3. $\phi_1 = \pi/2, \phi_2 = \pi/2$:
   $\Rightarrow |J| = 0,\ \Gamma = 2\Gamma_0,\ \theta = 0$. *Purely dissipative Lindbladian* dynamics.

4. $\phi_1 = 0, \phi_2 = \pi/2$:
   $\Rightarrow |J| = 1/\sqrt{2},\ \Gamma = \sqrt{2}\Gamma_0,\ \theta = \pi/4$. *Mixed dynamics, with characteristics of both Hermitian Hamiltonian evolution and dissipative Lindbladian evolution*.

6 Time-Reversal Symmetry Breaking in a Time-Multiplexed Resonator Network

In this section we clarify the remark from the main text that our network implements time-reversal symmetry breaking couplings.

Often, when one says that a system breaks time-reversal symmetry, what is mean is that it breaks time-reversal symmetry in a restricted sense [12]. One defines the system as a subsystem of the larger world and only considers the time-reversal of the system. A classic example of this is the motion of a charge in a constant magnetic field. It is commonly accepted that time-reversal symmetry is broken in such a system: if we reverse time, the direction of the magnetic field does not change. However, imagine that the magnetic field is generated by an electromagnet. If we include an electromagnet as a part of our system, then the magnetic field does change directions because the current in the electromagnet switches directions when we reverse time. Therefore, such a system only breaks time-reversal symmetry if we treat the source of the magnetic field as outside of our system.

Similarly, in our photonic network, we mean that our system breaks time-reversal symmetry in a restricted sense. As is standard practice in nonreciprocal photonic systems [12], we restrict our system to only consist of the photonic portion of the network. When we do this, some portions of our experiment, such as the modulator driving signals, are considered to be outside of our system, and they do not change when we reverse time in the system.

With this established, let us consider two ways in which our system breaks time-reversal symmetry.

One way to think about the time-reversal symmetry breaking in our dissipatively coupled system is as follows: Imagine light traveling clockwise in the dissipatively coupled resonators shown in Fig. 10(b). As light couples from the left resonator to the right resonator, some light is lost from the system through the open port because not all of the light in the bus waveguide is coupled into the right resonator. This loss is purely a feature of the dissipative coupling: Even if the resonators and the bus waveguides were lossless, this additional coupling loss would still be present. The presence of this coupling loss means that energy is not conserved in a pair of dissipatively coupled resonators, and, equivalently, time-reversal symmetry is broken.

However, it is important to note that this is a "trivial" time-reversal symmetry breaking. While dissipation inherently breaks time-reversal symmetry because it breaks energy conservation, this type of time-reversal symmetry breaking cannot endow our system with a nonzero Chern number. Therefore, our dissipatively coupled system requires another, "nontrivial" way of breaking time-reversal symmetry.

The second sense in which our system breaks time-reversal symmetry is in terms of the couplings. Consider the schematic representations of delay line couplings in a time-multiplexed network shown in Fig. 14. We consider three pulses traveling through delay lines of length $\pm T_{\mathrm{R}}$, as well as through the corresponding section of the main loop. In both delay lines we place phase modulators that control the coupling phases between the various pulses.

Let us first consider what happens when we run time forwards, as is illustrated in Fig. 14(a). The modulator in the $-T_{\mathrm{R}}$ delay line is programmed to couple Pulse 2 to Pulse 1 with a coupling phase of ϕ_1 and to couple Pulse 3 to Pulse 2 with a coupling phase of ϕ_2. The modulator in the $+T_{\mathrm{R}}$ delay line is programmed to couple Pulse 1 to Pulse 2 with a coupling phase of ϕ_3 and to couple Pulse 2 to Pulse 3 with a coupling phase of ϕ_4.

Next let us consider what happens when we reverse time in the network. While the pulses

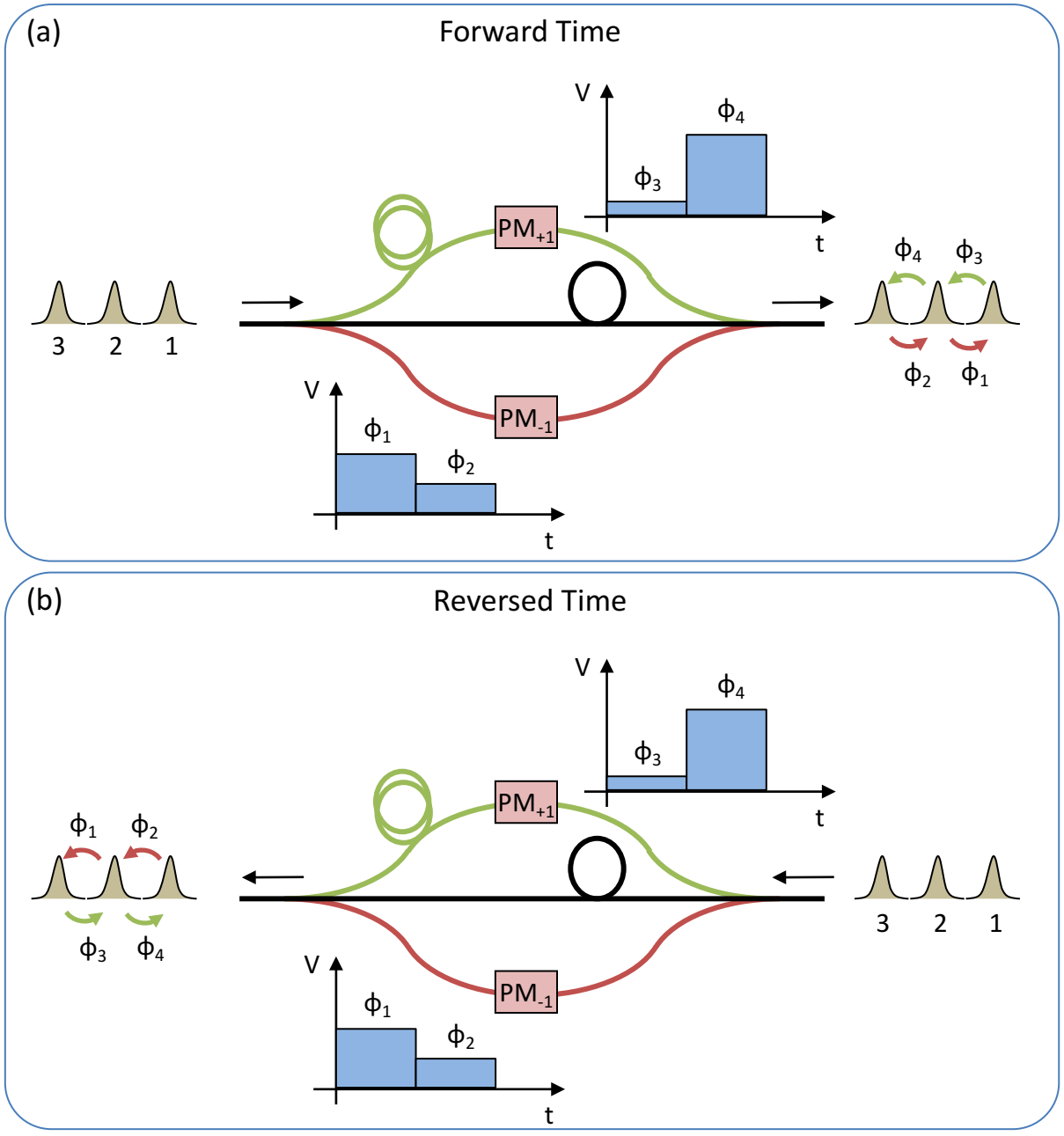

Figure 14: Time-reversal symmetry breaking in time-multiplexed networks. **(a)** Forward-time passage through the delay lines of a time-multiplexed network. **(b)** Time-reversed passage through the delay lines of a time-multiplexed network.

now propagate in the opposite direction through the delay lines, it is essential to note that two key things do not change. First, because the modulator driving signals are considered external to the system, we do not change the phase pattern imparted by the phase modulators in the delay lines. Second, we do not relabel our pulses. This is because each pulse is mapped to a specific lattice site in our synthetic lattice. When we reverse time, the order in which the synthetic lattice sites propagate through the delay lines changes, but the lattice sites retain their same positions in the synthetic lattice.

With this in mind, we can draw the phases acquired when the pulses propagate through the delay lines in a time-reversed fashion. This process is shown in Fig. 14(b). Now we see that Pulse 2 couples to Pulse 1 through the $+T_{\mathrm{R}}$ delay line with a phase of ϕ_4, while Pulse 3 couples to Pulse 2 through the $+T_{\mathrm{R}}$ delay line with a phase of ϕ_3. Through the $-T_{\mathrm{R}}$ delay line, Pulse 1 couples to Pulse 2 with a phase of ϕ_2 and Pulse 2 couples to Pulse 3 with a phase of ϕ_1. Note that these coupling phases are not the time-reversed phases of those encountered in the forward-time analysis.

This time-reversal symmetry breaking process is fundamentally different than the situation encountered in two passive, dissipatively coupled ring resonators, such as those shown in Fig. 10(b). The dynamics of two such resonators does not break time-reversal symmetry, for if the CW mode acquires a phase β as it couples from the left resonator to the right resonator, then the CCW mode also acquires the phase β as it couples from the second resonator to the first resonator. Therefore, in terms of the phases acquired by the CW and CCW modes, the CCW mode experiences the time-reversed dynamics of the CW mode. The system does still break time-reversal symmetry because of the nonlocal dissipation in the couplings, but as discussed above, this is a "trivial" time-reversal symmetry breaking.

What distinguishes our time-multiplexed system from the case of two spatially coupled resonators is that the modulators in our network are time-modulated. Because the modulators are driven by external signals, when we time-reverse the system, the system exhibits non-reciprocal behavior. However, if we remove this external drive, then the system becomes time-reversal symmetric. This can be seen directly from the system considered in Fig. 14: If one turns off the modulators so that the delay lines exhibit constant phases, then the system respects time-reversal symmetry. Note that this idea of using external modulation to break time-reversal symmetry is one way to construct a photonic isolator [13].

7 Ring-Down Measurement of the SSH Edge State

In the main text, we presented so-called steady-state measurements of the SSH and HH edge states. To perform these measurements, we repeatedly excited an edge state of the model under study and observed the steady-state behavior of the network. The degree of localization in the edge state once the system reached steady state allowed us to distinguish between the topologically trivial and nontrivial phases of the network. An alternative way to probe topological edge states in our network is to perform "ring-down" measurements, in which we excite a topological

edge state in our network and then observe the dynamics of the state as it decays in the network. As in the steady-state experiments, we expect that the topological edge state will remain localized in the excited edge state if the network is in the topological phase and that it will not if the network is in the trivial phase. In this section, we present ring-down measurements of the SSH edge state.

To perform the ring-down measurements in our network, we first prepare the couplings to be in either the topological or trivial phases with $w/v = 2$. We then excite the network with one of the theoretically expected edge states from the topological phase. We excite the network for 5 roundtrips to build up power in the network, and then we observe the decay of the excitation over another 15 roundtrips. The results of our measurement are shown in Fig. 15.

In Fig. 15(a), we plot the ring-down of the network in the topological phase as well as the final roundtrip on which we excite the network, which we label the 0th roundtrip. In Fig. 15(c), we plot the state of the network on the 10th roundtrip. We observe that the state of the network remains well localized in the excited topological edge state, which confirms that our network is in a topological phase. The small discrepancies between the theoretical edge state and the observed state are likely due to both inaccuracies in our network's couplings and nonlinear gain dynamics, which we will discuss shortly.

Similarly, in Fig. 15(b), we plot the ring-down of the network in the trivial phase. Now, by the 10th roundtrip, the state of the network deviates significantly from the excited topological edge state. In particular, rather than seeing light predominantly in alternate sites of our synthetic lattice, we see that the sites adjacent to the edges exhibit the second-highest occupation in the lattice. This provides strong evidence that the network is now in the trivial phase.

When we observe the network for more roundtrips in either the trivial or the topological phases, we find that gain fluctuations in the network degrade the visibility of the edge state excitation. In order to observe $\gtrsim 5$ roundtrips in our network, it is necessary for us to operate our network very close to threshold. This introduces some nonlinear gain dynamics in the system, which amplifies spurious pulses in the system after ~ 8 roundtrips. This effect is already noticeable in Fig. 15(c). Because the extinction ratio of the modulators at the input to the main cavity is imperfect, some light leaks into the cavity. When we operate very close to threshold, the EDFA in the main cavity can amplify these spurious pulses, causing the very slight bulk occupation visible in the figure. Moreover, the emergence of these spurious pulses in the bulk coincides with the incipient degradation of the excited edge state, which indicates that the discrepancies between the observed state in Fig. 15(c) and the theoretical edge state could be, in part, due to nonlinear gain dynamics. On successive roundtrips, the growth of these spurious pulses overwhelms the edge state excitation, and the topological edge state is no longer visible. However, before these nonlinear gain dynamics dominate the system, the system decays exponentially and remains localized in the initially excited edge state, as we would expect in the linear case. This suggests that the linear dynamics govern the initial dynamics of the system.

The degree to which the state of the network deviates from the edge state excitation in the trivial case is limited primarily by the gain and loss in the network. As mentioned above, near threshold, nonlinear gain dynamics prevents us from observing the dynamics of the excitation

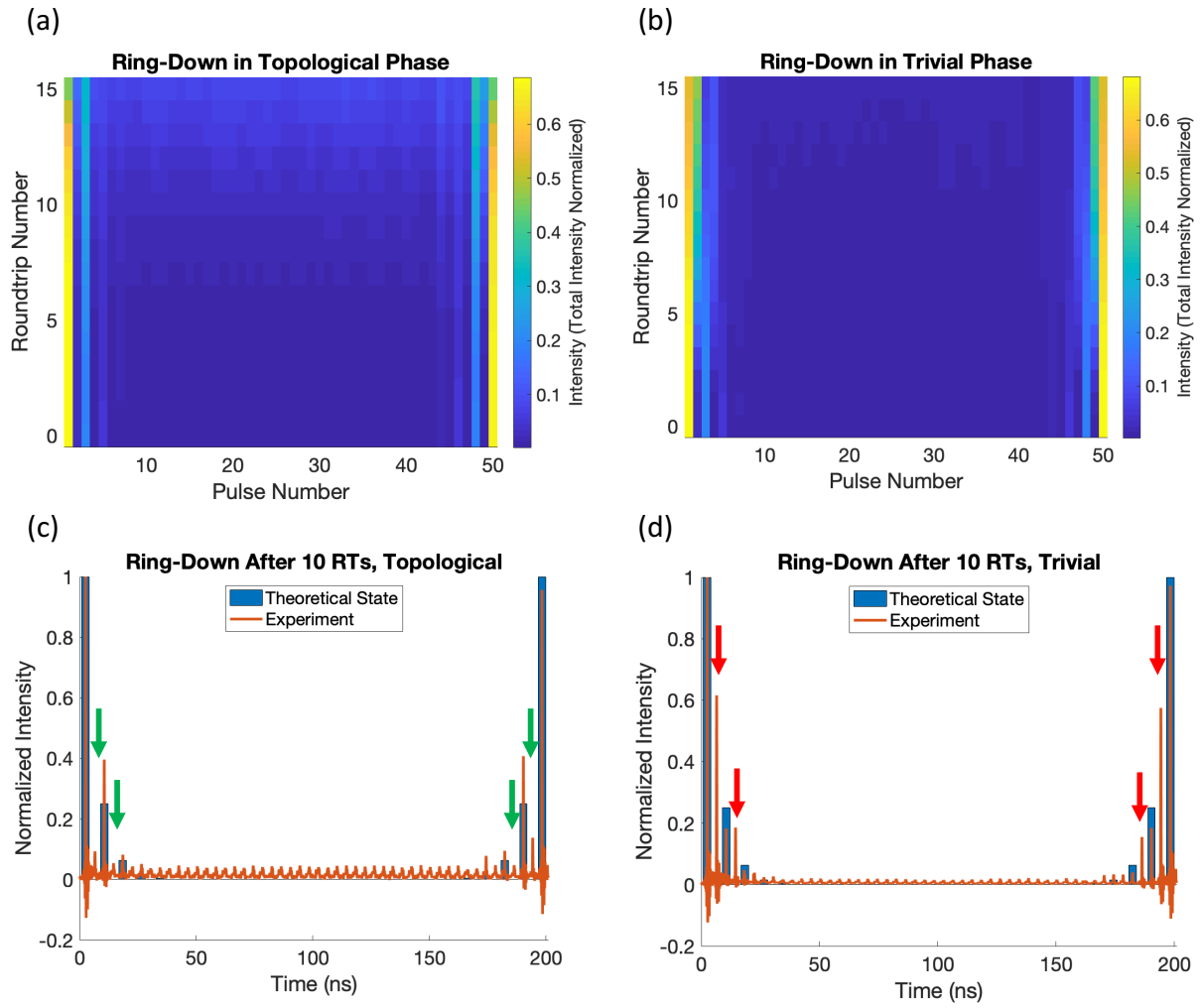

Figure 15: Ring-down measurements of the SSH edge state. **(a)** Ring-down measurement in the topological phase. Each cell of the plot represents the peak power of the pulse at that location and roundtrip. To show how the power spreads between the pulses of the network, the vector comprised of the plotted peak powers is normalized on each roundtrip. **(b)** Ring-down measurements in the trivial phase. **(c)** Time trace of the network state on the 10th roundtrip in the topological phase. The state of the network closely resembles the theoretical topological edge state, which indicates that the network is in the topological phase. **(d)** Time trace of the network state on the 10th roundtrip in the trivial phase. As expected, the state no longer resembles the theoretical topological edge state of the SSH model.

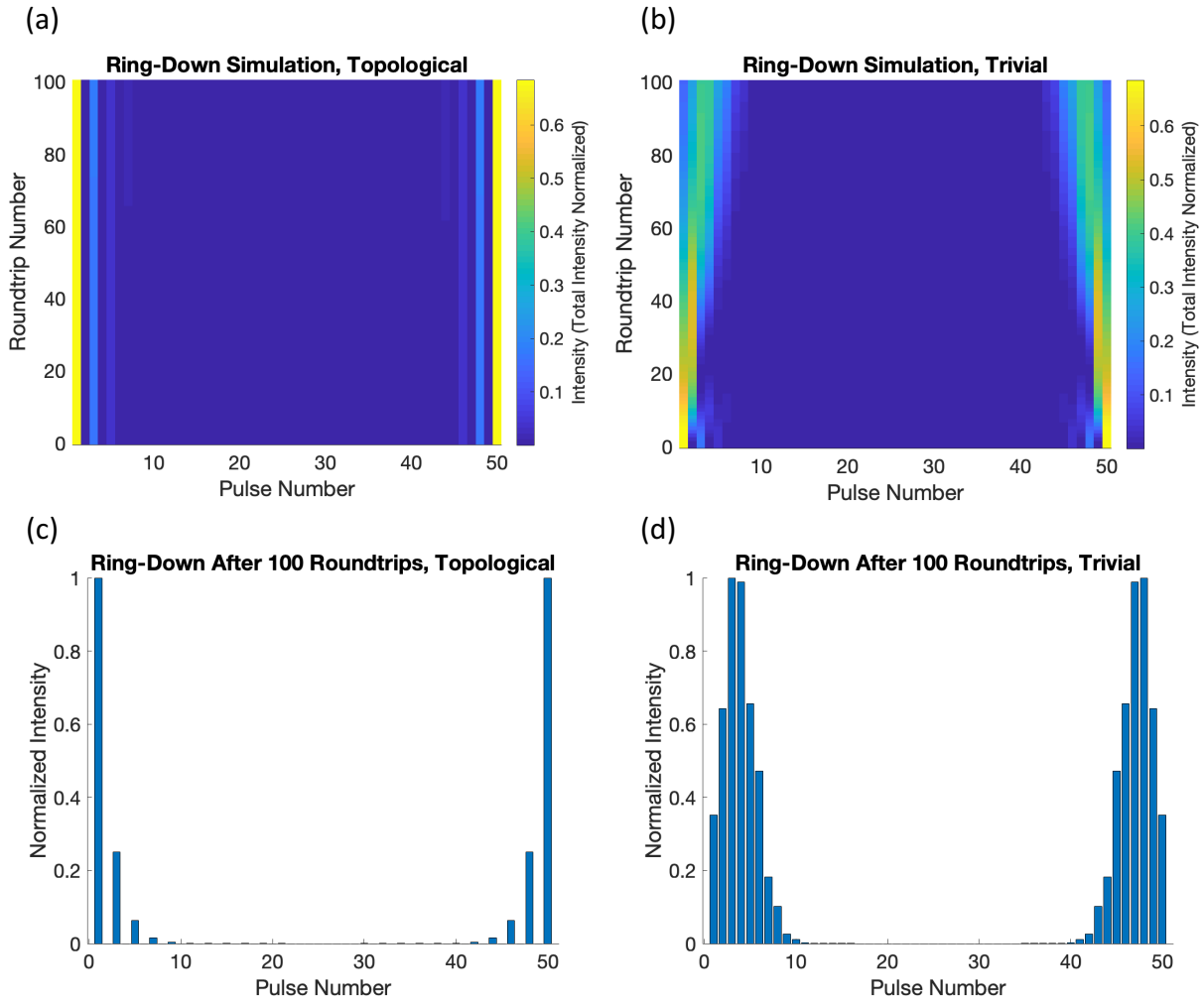

Figure 16: Simulation of the SSH ring-down experiment. **(a)** Simulation of the ring-down experiment over 100 roundtrips in the topological phase. **(b)** Comparable simulation in the trivial phase. **(c)** State of the topological network on the 100th roundtrip. **(d)** State of the trivial network on the 100th roundtrip. Note that the normalizations in this figure are the same as those in Fig. 15.

for more roundtrips than what is shown in Fig. 15. Farther below threshold, loss limits the number of roundtrips we can observe because the system quickly drops below the noise floor of our detector. The difficulty of observing more roundtrips limits the degree to which we observe the edge state spreading into the bulk. In Fig. 16, we simulate our ring-down experiments over 100 roundtrips. In these simulations we observe significantly more penetration into the bulk in the trivial phase.

Note that the simulations in Fig. 16 are performed by simulating the discrete time version of Eq. 12,

$$\mathbf{a}_{n+1} = (K - \gamma)\,\mathbf{a}_n, \tag{54}$$

where K implements of the couplings of the model under study (here the SSH model) and $\mathbf{a}_0$ is chosen to be a topological edge state of the model. Each iteration of the difference equation in Eq. 54 models the roundtrip dynamics of our time-multiplexed network. For the simulations in Fig. 16 we must specify three parameters, which are the SSH coupling strengths w and v and the roundtrip loss γ. For the simulations in Fig. 16 we use $w = 0.1$, $v = 0.05$, and $\gamma = 0.25$.

8 Simulations of Topological Robustness in an HH Lattice with Purely Dissipative Couplings

In Fig. (6) of the main text, we presented simulations of topological edge states in a 4×10 HH lattice with and without a defect introduced on the corner of the lattice. Here we discuss how topological robustness manifests in dissipatively coupled HH lattices and discuss the details of the simulations presented in the main text. We also provide additional simulations that show the topological robustness of the HH edge state in a 20×20 dissipatively coupled HH lattice.

In a system with purely dissipative couplings, we cannot observe topological protection in the same manner as in conservatively coupled systems [14]. In conservatively coupled HH lattices, one may observe robustness by removing a site on the edge of the lattice to introduce a defect. One may then excite the system with a frequency in the system's bandgap and observe that the excitation propagates around the defect without backscattering. However, as discussed in Supplementary Sec. 3, in systems with purely dissipative couplings, there is no topological transport, and therefore we would not expect to see propagation around an edge defect in our system.

With that said, in the presence of a defect, the topology of our dissipatively coupled system still guarantees the existence of topological edge states in the presence of a defect or in the presence of any disorder that does not close the dissipative topological bandgap. This is a direct consequence of the bulk-boundary correspondence [15]: The difference in topological invariants between the lattice and the surrounding vacuum guarantees the existence of localized states at the boundary, regardless of the boundary's shape. The dynamics of these states, whether conservative or dissipative, does not influence the *existence* of the edge states.

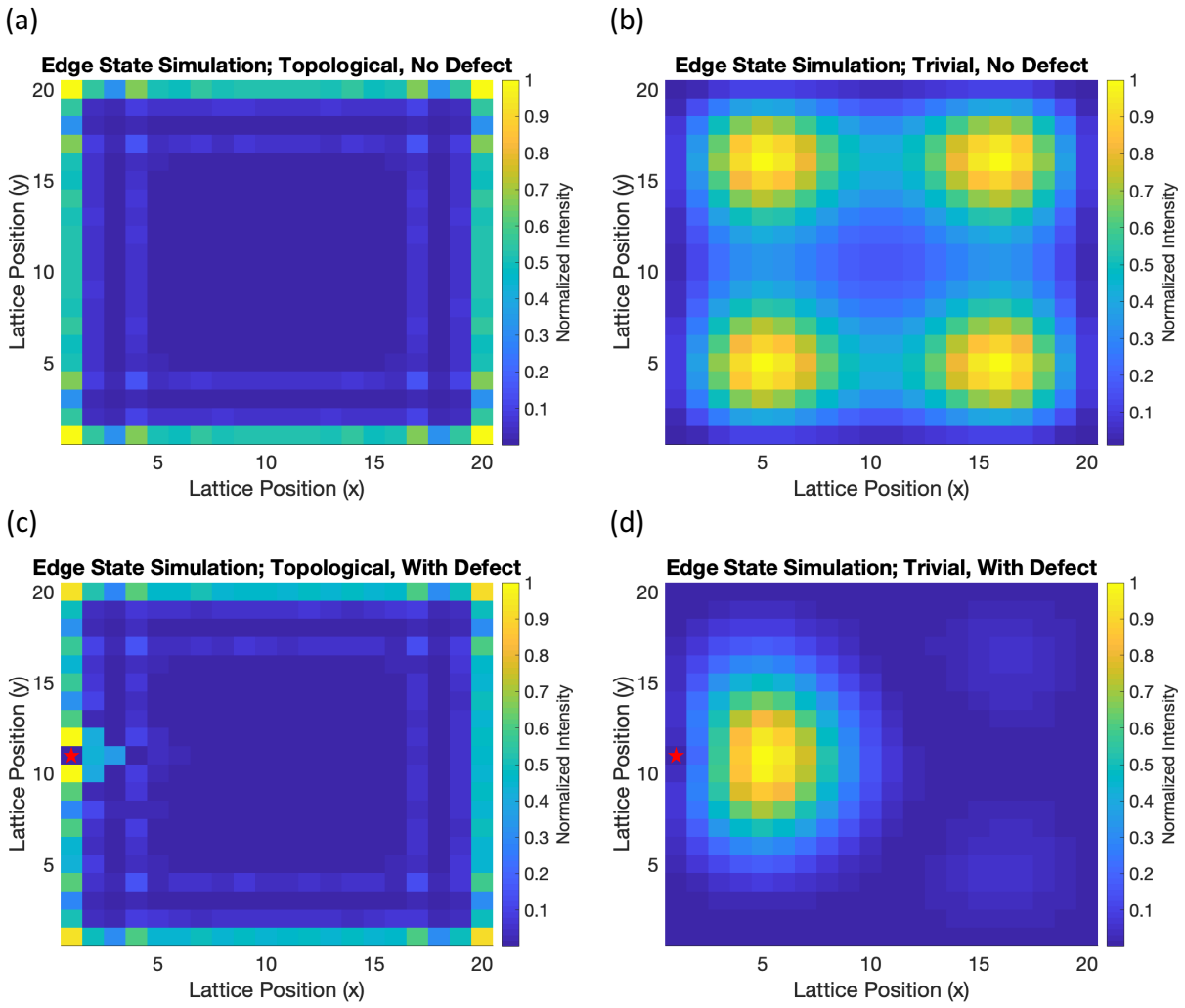

Figure 17: Simulations of an HH ring-down experiment. Each simulation shows the evolution of an edge-state excitation after 100 roundtrips in a dissipatively coupled HH synthetic lattice. **(a)** Simulation in a topological lattice with no defect. **(b)** Simulation in a trivial lattice with no defect. **(c)** Simulation in a topological lattice with a defect. **(d)** Simulation in a trivial lattice with a defect. Note that the location of the defect is indicated in **(c,d)** by a small red star on the left edge.

Because the HH edge states are guaranteed to exist in the presence of defects or disorder, we can imagine probing the HH edge states that emerge in these disordered lattices using the same experimental procedures discussed in this text. Here and in the main text, we show simulations of ring-down experiments similar to those discussed in Supplementary Sec. 7. In our simulations we excite our network with the HH edge state that exists either in the presence of a defect or in the absence of a defect. With a synthetic magnetic field either on or off, we let the edge state excitation evolve for 100 roundtrips and record the final state of the network.

The results of ring down simulations for a 20×20 HH lattice are shown in Fig. 17. The final state in each plot is normalized by dividing the final state by the maximum intensity. Note that the simulations in the main text are normalized in the same manner. In Fig. 17(a), we show the final state for the HH lattice with a synthetic magnetic field of $\alpha = 1/3$. As expected, the final state observed in this figure is indistinguishable from the edge state excitation. When we turn off the synthetic magnetic field ($\alpha = 0$), the edge state excitation no longer remains localized at the edge. After 100 roundtrips, the initial excitation "diffuses" entirely into the bulk of the lattice, which correctly indicates that the system is in a trivial phase.

In Fig. 17(c), we introduce a defect in the left edge of the dissipatively coupled lattice. In the figure, the location of the defect is marked by a small red star on the left edge. As guaranteed by the bulk-boundary correspondence, topological edge states appear at the boundary of the new lattice. When we excite one of these edge states in the presence of a synthetic magnetic field ($\alpha = 1/3$), the system remains in the excited edge state, and the final state in Fig. 17(c) is indistinguishable from the excitation. Finally, when we turn off the synthetic magnetic field in the presence of the defect, we again observe that the edge state excitation no longer remains localized at the edge of the lattice, as the system is now in a trivial phase.

Note that for the simulations performed in Fig. 17 and in Fig. 6 of the main text, we again simulate Eq. 54, but now we choose K to implement the HH model. For these simulations we must specify the coupling strength of the HH model J, the strength of the effective magnetic field α, and the roundtrip loss in the network γ. For the simulations here and in the main text we choose $J = 0.2$ and $\gamma = J$. We switch α between $1/3$ and 0 depending on whether the lattice is topological or trivial.

References

[1] FPGA source code and documentation. https://github.com/fluorine21/RFSoC_Controller.

[2] Black, E. An introduction to Pound-Drever-Hall laser frequency stabilization. *Am. J. Phys.* **69**, 79 (2001).

[3] Aster, R. C., Borchers, B. & Thurber, C. H. *Parameter Estimation and Inverse Problems* (Elsevier Science and Technology, 2013), 2 edn.

[4] Ozawa, T., et al. Topological photonics. *Rev. Mod. Phys.* **91**, 015006 (2019).

[5] Xu, Q. *et al.* Experimental realization of an on-chip all-optical analogue to electromagnetically induced transparency. *Phys. Rev. Lett.* **96**, 124901 (2006).

[6] Mancinelli, M. *et al.* Coupled-resonator-induced-transparency concept for wavelength routing applications. *Opt. Express, OE* **19**, 12227–12240 (2011). Publisher: Optical Society of America.

[7] Smith, D. D., Chang, H., Fuller, K. A., Rosenberger, A. T. & Boyd, R. W. Coupled-resonator-induced transparency. *Physical Review A* **69**, 063804 (2004).

[8] Maleki, I., Matsko, A., Savchenkov, A. & Ilchenko, V. Tunable delay line with interacting whispering-gallery-mode resonators. *Opt. Lett.* **29**, 626–628 (2004).

[9] Peng, B., Özdemir, Ş. K., Chen, W., Nori, F. & Yang, L. What is and what is not electromagnetically induced transparency in whispering-gallery microcavities. *Nat. Commun.* **5**, 5082 (2014).

[10] Asbóth, J., Oroszlány, L. & Pályi, A. *A Short Course on Topological Insulators* (Springer, 2016), 1 edn.

[11] Wanjura, C. C., Brunelli, M. & Nunnenkamp, A. Topological framework for directional amplification in driven-dissipative cavity arrays. *Nature Communications* **11**, 3149 (2020).

[12] Asadchy, V., Mirmoosa, M., Diaz-Rubio, A., Fan, S. & Tretyakov, S. Tutorial on electromagnetic nonreciprocity and its origins. *Proc. IEEE* **108**, 684–1727 (2020).

[13] Doerr, C., Dupuis, N. & Zhang, L. Optical isolator using two tandem phase modulators. *Opt. Lett.* **36**, 4293–4295 (2011).

[14] Hafezi et al., M. Robust optical delay lines with topological protection. *Nat. Phys.* **7**, 907 (2011).

[15] Hatsugai, Y. Chern number and edge states in the integer quantum Hall effect. *Physical Review Letters* **71**, 3697–3700 (1993).